Supplementary Information

Nonplanar tertiary-N extended nitrobenzene enables insoluble and low-energy-barrier organic small molecule cathode for high-performance aqueous batteries

Ziyang Song,[a,b,c] Qi Huang,[d] Yaokang Lv,[e] Lihua Gan,[a,c] Mingxian Liu[a,c,*]

[a] School of Chemical Science and Engineering, State Key Laboratory of Cardiovascular Diseases and Medical Innovation Center, Shanghai East Hospital, Tongji University, 1239 Siping Road, Shanghai 200092, China. *E-mail: liumx@tongji.edu.cn

[b] State Key Laboratory of Water Pollution Control and Green Resource Recycling, College of Environmental Science and Engineering, Advanced Research Institute, Tongji University, 1239 Siping Road, Shanghai 200092, China.

[c] Shanghai Key Lab of Chemical Assessment and Sustainability, Shanghai 200092, China.

[d] State Key Laboratory of Photovoltaic Science and Technology, Institute of Optoelectronics, College of Future Information Technology, Fudan University, Shanghai 200438, China.

[e] College of Chemical Engineering, Zhejiang University of Technology, 18 Chaowang Road, Hangzhou 310014, China.

Section S1. Experimental Process

1.1 Materials

All reagents were commercially available and directly used. *N*,*N*,*N*′,*N*′-tetrakis(4-nitrophenyl)-1,4-benzenediamine (TNB, 98%), 1,4-dinitrobenzene (DB, 98%) and trisphenylamine (TA, 98%) were directly purchased from Aladdin without further purification. $ZnSO_4$ salt was purchased from Titan.

1.2 Characterizations

Nuclear magnetic resonance (NMR) spectra were performed in DMSO-d_6 on Bruker AV-500 (^{1}H 400 MHz). Fourier-transformed infrared spectra (FT-IR) were collected through a Thermo Nicolet NEXUS spectrometer. The geometries of organics were recorded by scanning electron microscopy (SEM) and transmission electron microscopy (TEM) images. X-ray diffraction (XRD) pattern was performed to observe the structures of samples using a Bruker D8 advance powder diffractometer (Cu Kα radiation source). The ultraviolet visible (UV-Vis) spectra were monitored by a UV-Vis spectrometer (JASCO V-750). The electrical conductivity test was performed by an RTS-8 four-point probe. X-ray photoelectron spectrometer (XPS, AXIS Ultra DLD) was applied to investigate the chemical composition. For the conductivity test, TNB was placed in the round mold (1 cm in diameter), and then was pressed into a thin sheet (diameter: 1 cm; thickness: 0.1 cm) on the RTS-8 four-point probe.

1.3 Electrochemical Tests

To fabricate organic cathodes, a mixture of TNB (or DB, TA), acetylene black and polytetrafluoroethylene (with a mass ratio of 6:3:1) was compressed into discs and pressed onto stainless-steel mesh. Then, the cathodes were dried at 60 °C for 12 h under a vacuum condition. The mass loading of TNB on the cathode is 3.5 mg cm^{-2}. Following the same procedure, a practical-level mass loading of 12.7 mg cm^{-2} for TNB in the cathode was also fabricated.

To construct aqueous Zn-organic batteries (ZOBs), TNB cathode (size/mass loading: 3.5 mg cm^{-2}), 3 mol L^{-1} aqueous $ZnSO_4$ electrolyte (120 μL), Zn metal anode (>99.99% purity; 100 μm in thickness), and glass fiber separator (Whatman) were packaged into

2032 coin-type cells. Galvanostatic charge/discharge (GCD) profiles and cyclic stability of ZOBs were tested on a LAND-CT3002A battery test system. Cyclic voltammetry (CV) and electrochemical impedance spectroscopy (EIS) tests were carried out on a CHI660E electrochemical workstation. The specific capacity (C_m, mAh g^{-1}) was calculated from GCD curves according to the following equations:

$$C_m = \frac{I \times \Delta t}{m} \quad \text{(Eq. S1)}$$

where I, Δt, m represents the current density (A g^{-1}), discharging time (s) and mass loading of active materials in cathodes, respectively.

The gravimetric energy density (E, Wh kg^{-1}) and power density (P, W kg^{-1}) of ZOBs were calculated according to the following equations:

$$E = C_m \times \Delta V \quad \text{(Eq. S2)}$$

$$P = \frac{E}{1000 \times \Delta t} \quad \text{(Eq. S3)}$$

where ΔV is the voltage window. The electrochemical metrics including specific capacities and energy/power densities were estimated based on the mass loading of active materials in the cathode.

Section S2. Calculation Methods

2.1 Computational Details.

Molecular Property Simulation. Density functional theory (DFT) calculations were performed with the Gaussian 16 software package.[S1−S4] Geometrical optimizations were conducted at the B3LYP-D3/ def2-SVP level of theory. The water solvent was included in the calculations using the solvation model based on the density (SMD) model. The π-electron localization function (ELF-π) and localized orbital locator function (LOL-π) calculation were performed via Multiwfn 3.8 programs.

Molecular Dynamics Simulation Details. The initial configurations of the systems were constructed by using the Packmol software.[S5] The theorical simulations were performed using GROMACS package (version 2019.3)[S6-9] with the all-atom OPLS (optimized performance for liquid systems) force field.[S10] Water molecules were described using the simple point charge/extend (SPC/E) model.[S11] For each system, the steep descent method was employed to minimize the system energy. Subsequently, molecular dynamics simulations under NPT ensemble at 298 K and 1 atm were conducted for 100 ns for each system. LINCS algorithm was applied to constrain the bond lengths of other components.[S12] Periodic boundary conditions were applied in all three directions. The temperature remains constant using the V-rescale thermostat algorithm.[S13] The cut-off distance for the Lennard-Jones and electrostatic interactions was 1.2 nm. Particle mesh Ewald method[S14] was used to determine the long-range electrostatic interactions. Configurations were visualized using Visual Molecular Dynamics software.[S15]

Several structures were taken from the finial simulated configurations. Then the single-point energies of complexes were calculated using the density functional theory (DFT) at the ωB97XD/def2-SVP level.[S15] Gaussian 16 package, revision A. 01 were used to perform the calculations. The binding energy (ΔE) of the configuration was calculated by the following equation:

$$\Delta E = E_{AB} - (E_A + E_B) \qquad \text{(Eq. S4)}$$

where E_A, E_B and E_{AB} mean the energies of A (one $ZnSO_4$ or one water molecule), B (excluding fragment A), and the total energy, respectively. A negative value of ΔE suggests that the reaction process is exothermic, and a higher negative value corresponds to a stronger interaction, which implies more heat release and a more stable structure.

Energy Barrier Calculation. The binding energy between anion/cation and TNB were calculated using the Vienna Ab initio Simulation Package (VASP)[S16] with the projector augmented wave (PAW) method[S17]. The exchange-functional was treated using the generalized gradient approximation (GGA) with Perdew-Burke-Emzerhof (PBE)[S18] functional. The charge density differences were simulated by VASPKIT code. The charge density differences between anion/cation and TNB model were simulated, and the charge transfer level between both was calculated by Bader charge analysis.[S19]

2.2 Optical Energy Gap.

The optical energy gaps (E_g) of organics were calculated through UV-Vis spectra based on the following equations:[S20]

$$\alpha \propto \frac{(h\nu - E_g)^{1/2}}{h\nu} \quad \text{(Eq. S5)}$$

$$h\nu = 1280/\lambda \quad \text{(Eq. S6)}$$

where α is the optical absorption coefficient, $h\nu$ is the photon energy, λ is the wavelength. The unit of E_g is eV.

2.3 Activation Energy.

The activation energy (E_a) for the charge transfer process was calculated by the Arrhenius equation:[S21]

$$\ln(R_{ct}^{-1}) = -E_a/RT + k \quad \text{(Eq. S7)}$$

where R_{ct}, is the charge transfer resistance (Ω), R is the gas constant (8.314 J mol^{-1} K^{-1}), T is the experimental temperature (K), k is a constant. The unit of E_a is eV

2.4 Capacitive Contribution.

The charge storage kinetics of ZOBs were investigated based on the equation:[S22]

$$i = kv^b \quad \text{(Eq. S8)}$$

where k and b refer to constants, i and v are current density and scan rate, respectively. When the power exponent b value is close to 0.5, it identifies a diffusion-controlled process, while a b-value of 1.0 suggests a surface-dominated redox reaction process.[S17]

The Dunn's method was applied to analyze the capacitive contribution from the rapid surface redox capacitive process and the diffusion-limited process.

Quantitative capacitive contribution can be calculated according to the equation:[S23]

$$i = k_1v + k_2v^{1/2} \quad \text{(Eq. S9)}$$

where k_1 and k_2 are constants, k_1v and $k_2v^{1/2}$ are the current density contributed from fast-capacitive process and diffusion-controlled process, respectively. Dividing $v^{1/2}$ on both sides of the above equation gets:

$$i/v^{1/2} = k_1v^{1/2} + k_2 \quad \text{(Eq. S10)}$$

In general, $i/v^{1/2}$ and $v^{1/2}$ show a linear relationship, two capacity contributions can be separated by linear fitting. The slope belongs to k_1 and the y-intercept equals k_2. By repeating the above steps for other voltages and sweep rates, the respective capacity contribution from the surface-controlled process and a diffusion-controlled process can be quantitatively calculated.

2.5 Redox Electron Transfer Number.

The theoretical capacity (C_m, mAh g^{-1}) of an organic cathode can be calculated based on the form:[S24]

$$C_m = \frac{n \times F}{3.6 \times M} \quad \text{(Eq. S11)}$$

where F is a constant (96485 C mol^{-1}), M is the molar mass of an organic material (g

mol^{-1}). Considering the molecular mass (*M*) of the tertiary-N extended nitrobenzene unit of 592.52 g mol^{-1} and the electron transfer number (*n*) of 10, the theoretical capacity of TNB is calculated to be 452 mAh g^{-1}.

Of note, the capacity-voltage and cycling stability of various organic cathodes was compared by prioritizing literature results tested generally under identical testing conditions (active mass loading: 1.5~3.0 mg cm^{-2}; potential window: 0.2~1.6 V; current density: 0.2~0.3 A g^{-1} for the capacity-voltage contour map and 5~10 A g^{-1} for cycling life comparison; electrolyte: aqueous zinc salt solution) for objective electrochemical evaluation.

For XPS characterizations (Fig. 3d−f), TNB cathode was collected by disassembling the battery at a specific potential during (dis)charging. After that, TNB cathode was rinsed thoroughly with distilled water to ensure the removal of adhered glass fiber and residual electrolyte. Finally, the cathode was dried at 60 °C in a vacuum oven to obtain a clean surface for spectroscopic analysis.

Section S3. Supplementary Characterizations

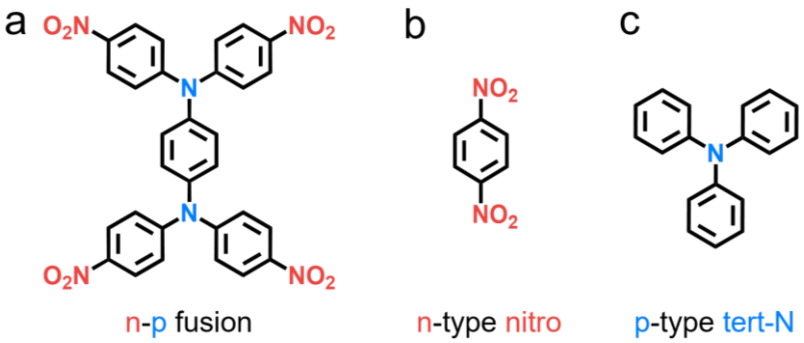

Fig. S1 Molecular structures of (a) extended nonplanar TNB, (b) planar DB and (c) nonplanar TA.

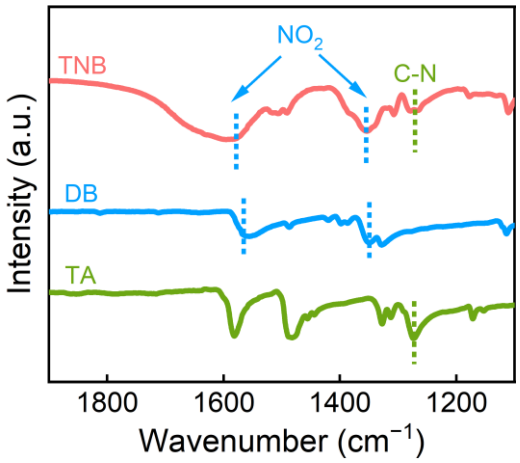

Fig. S2 FT-IR spectra of TNB, DB and TA compounds.

Notes: FT-IR spectra exhibit the presence of C−N groups at 1272 cm^{-1} in TA and TNB, and NO_2 groups at 1587/1352 cm^{-1} in DB and TNB. These results indicate the redox ambipolarity of TNB with dual NO_2 and C−N active sites.

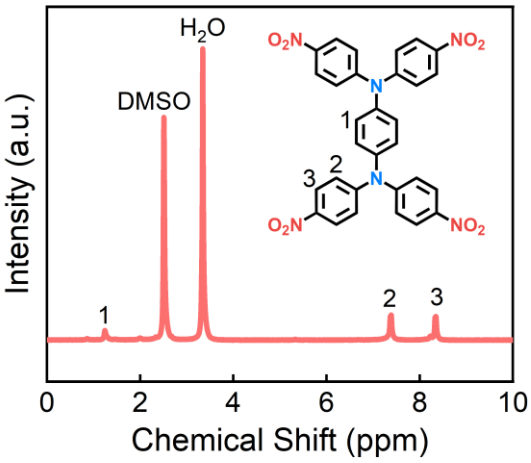

Fig. S3 ^{1}H NMR spectrum of TNB.

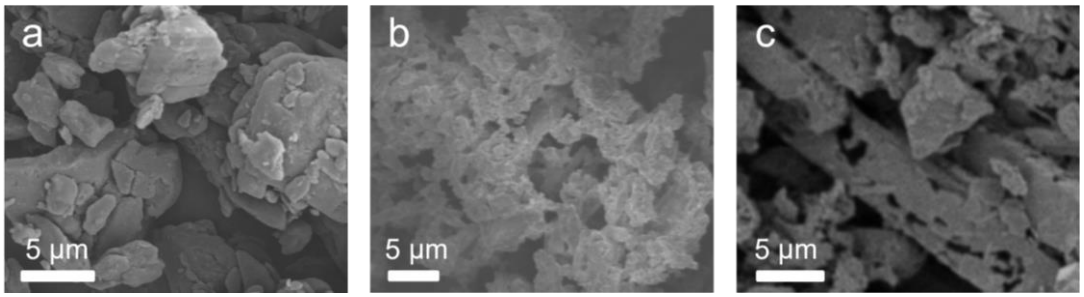

Fig. S4 SEM images of (a) TNB, (b) DB and (c) TA.

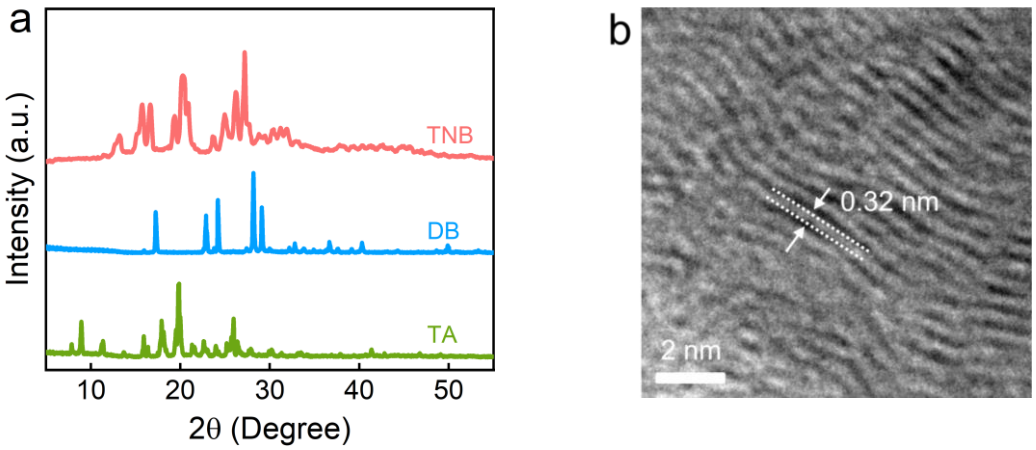

Fig. S5 (a) XRD patterns of TNB, DB and TA molecules. (b) High-resolution TEM image of TNB.

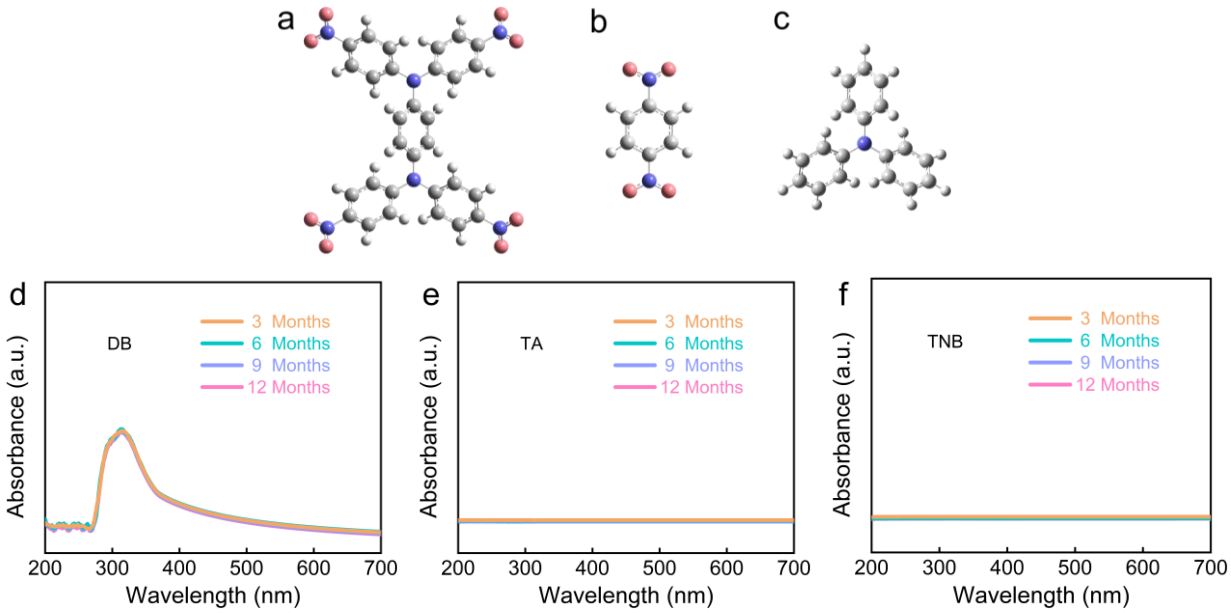

Fig. S6 Optimized molecular structures of (a) TNB, (b) DB and (c) TA. UV-Vis spectra of 3 M $ZnSO_4/H_2O$ electrolyte after immersing (d) DB, (e) TA and (f) TNB compounds for 3−12 months.

Notes: DB, TA and TNB compounds were soaked in 3 M $ZnSO_4/H_2O$ electrolyte for 3−12 months, and their solubility was further assessed by ultraviolet-visible (UV-Vis) spectrum analysis (Fig. S6d−f). DB shows obvious dissolution signal in UV-Vis spectrum, with an assessed solubility of 4.62 mmol L^{-1}, indicating its structural instability in the aqueous electrolyte. In contrast, no absorption peaks can be observed in UV-Vis spectra for TA and TNB compounds, so their concentration are 0 mmol L^{-1}, highlighting their nonplanar structural stability.

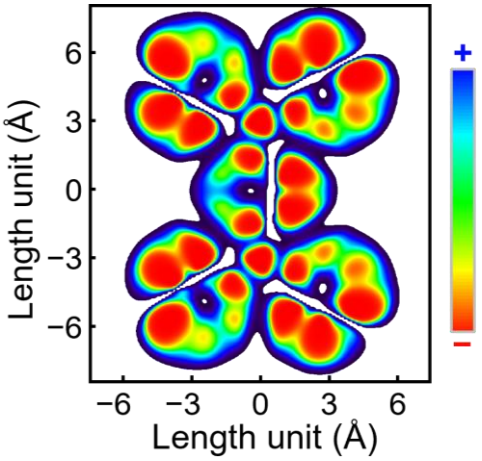

Fig. S7. LOL-π image of TNB.

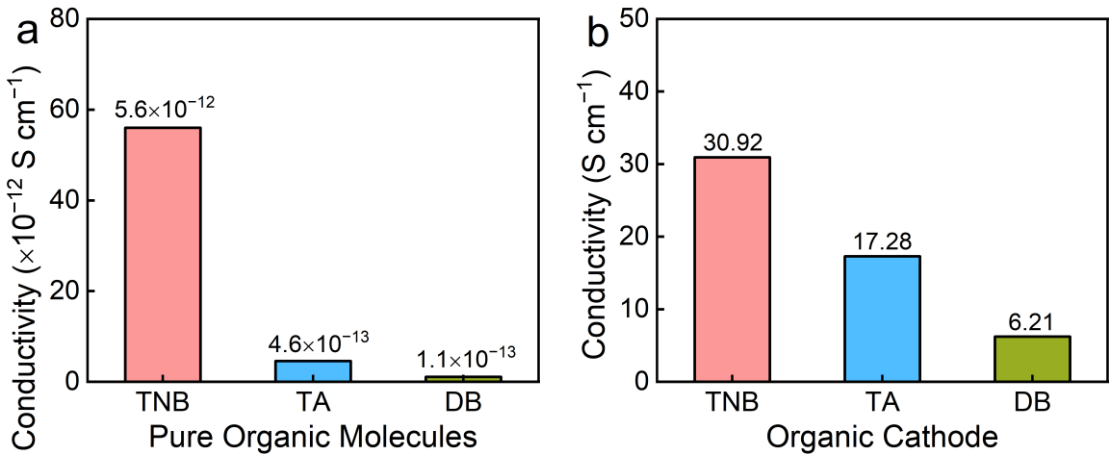

Fig. S8 (a) Electrical conductivities of three pure organic molecules. (b) Electrical conductivities of three organic cathode materials.

Notes: Based on the four-probe testing method, the intrinsic electrical conductivity of pure TNB, TA and DB molecules are 5.6×10^{-12}, 4.6×10^{-13} and 1.1×10^{-13} S cm^{-1} (Fig. S8a), respectively. With the addition of acetylene black conductive agent (30 wt%), the electronic conductivity of TNB cathode is assessed to be 30.92 S cm^{-1} (Fig. S8b). The formation of an efficient conductive network does a favor to efficient interfacial electron transfer efficiency to promise high utilization of active-sites in the cathode and thus high capacity.

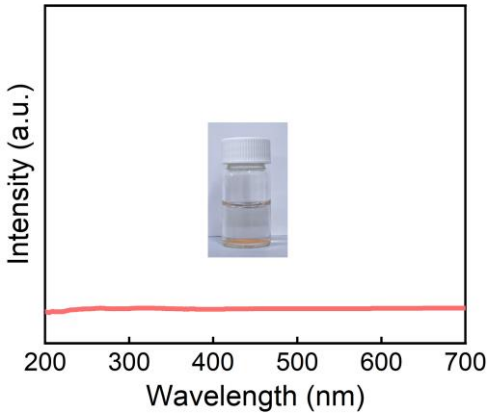

Fig. S9 UV-Vis spectrum and digital photograph of 3 M aqueous $ZnSO_4$ electrolyte soaked with TNB for twelve months.

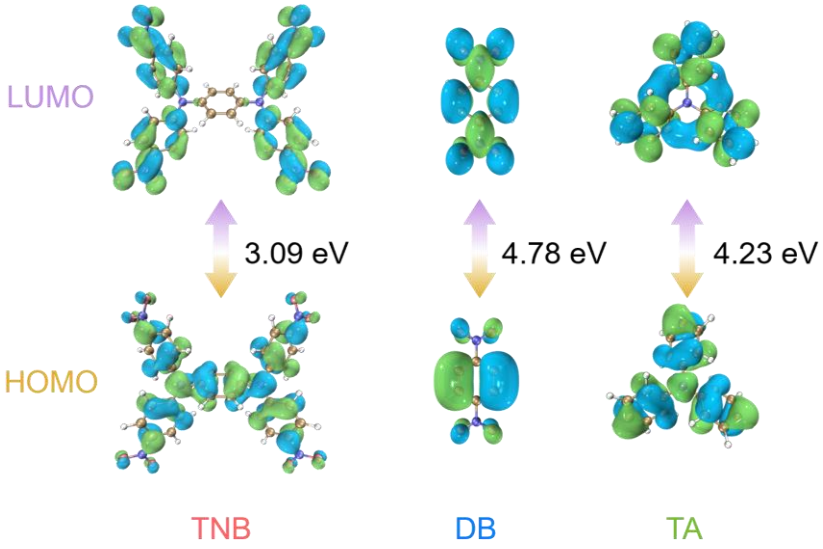

Fig. S10 Energy levels and frontier molecular orbitals of TNB, DB and TA.

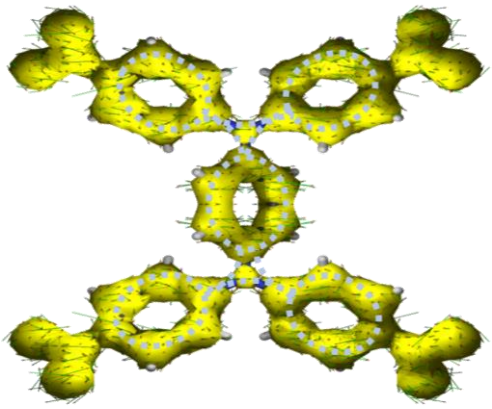

Fig. S11 The anisotropy of the induced current density (ACID) plots of TNB.

Notes: ACID calculation shows that the diamagnetic continuous current flows over the backbone of TNB, implying its high structure conjugation and π-aromaticity for supporting fast and stable electron transfer.

Section S4. Electrochemical Results

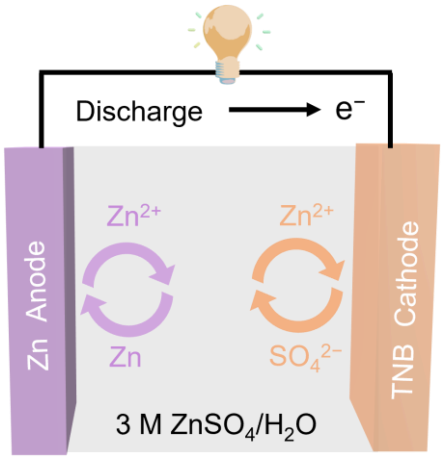

Fig. S12 Schematic configuration of Zn||TNB cell, including Zn metal anode, 3 M $ZnSO_4/H_2O$ electrolyte, and TNB cathode.

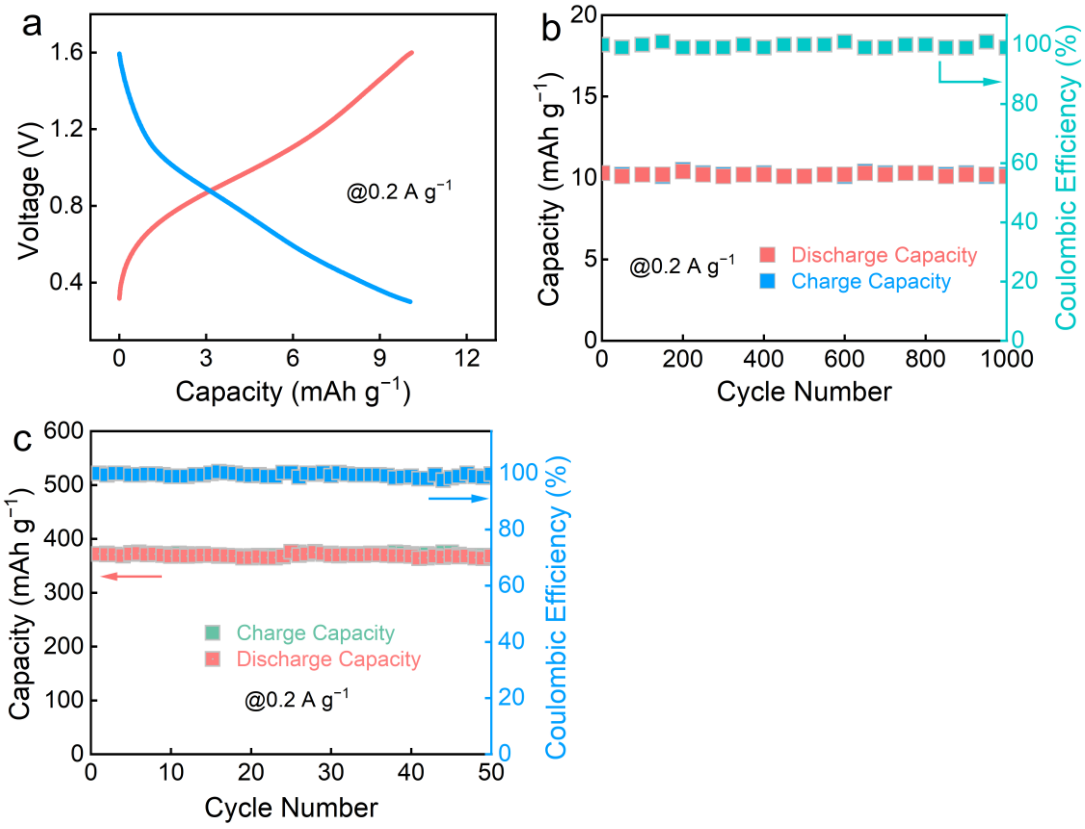

Fig. S13 (a) GCD profile and (b) cycling performance of Zn||acetylene black battery using 3 M $ZnSO_4/H_2O$ electrolyte. (c) Electrochemical capacities of TNB cathode (TNB:acetylene:PTFE = 7:2:1).

Notes: The conductive agent of acetylene black shows an insignificant capacity

contribution of 10 mAh g^{-1}. TNB cathode with 20 wt% acetylene black conductive additive (TNB:acetylene:PTFE = 7:2:1) shows an electrochemical capacity of 372 mAh g^{-1} at 0.2 A g^{-1}, which is lower than that of the original formulation (6:3:1, 30 wt% conductive additive, 430 mAh g^{-1}). The reduced capacity is primarily attributed to the lower electronic conductivity of TNB cathode with less conductive carbon, which increases the redox reaction resistance and decreases the utilization efficiency of the redox-active sites.

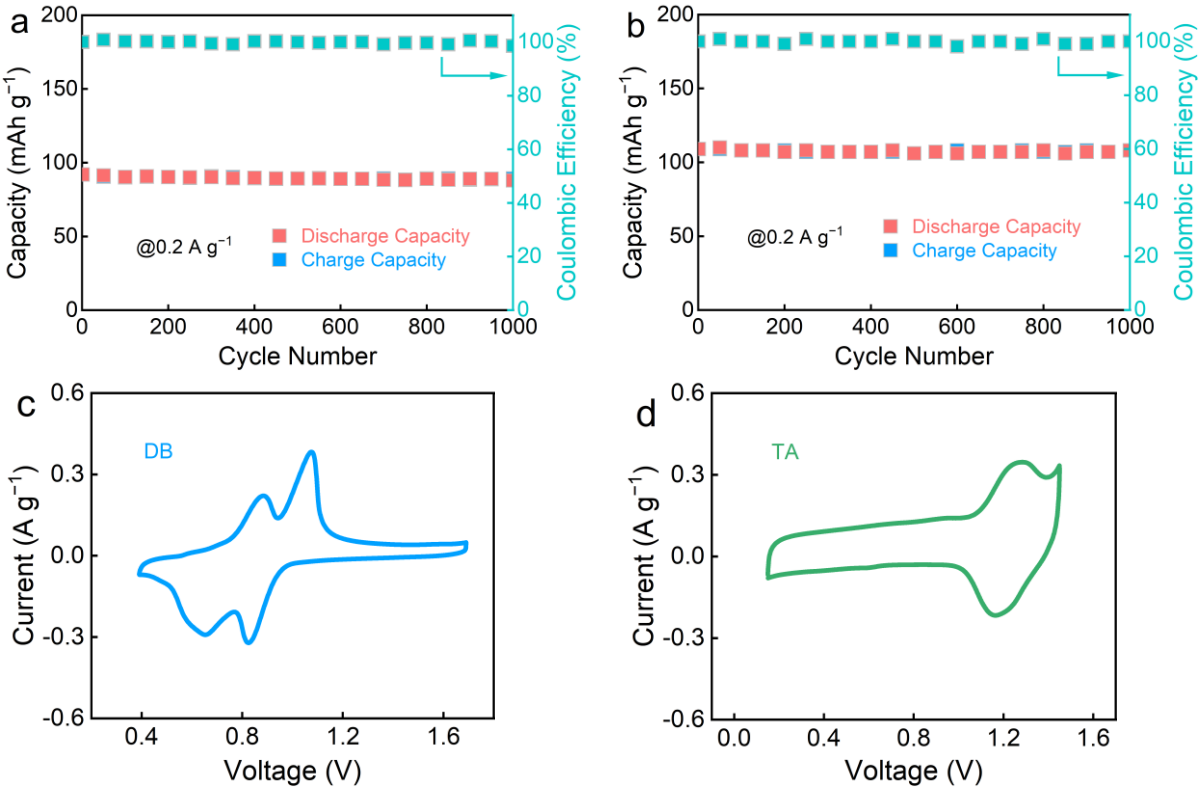

Fig. S14 (a, b) Cycling stability and (c, d) CV profiles of (a, c) Zn||DB and (b, d) Zn||TA batteries using 3 M $ZnSO_4/H_2O$ electrolyte.

Notes: CV profile of TA cathode shows a pair of redox peaks (1.27/1.17 V), which conforms to the redox signals of TNB cathode at high-potential region. This result reveals the p-type tert-N redox activity of TNB, which can accommodate SO_4^{2-} anion. Furthermore, two pairs of redox signals (0.89/0.65 and 1.08/0.82 V) of CV curve of DB cathode agree with TNB cathode at low-potential region, indicating the n-type nitro redox activity for two-step successive Zn^{2+} coordination. These results indicate that SO_4^{2-} anions and Zn^{2+} cations dominate the energy storage of TNB cathode by the stepwise redox reaction with tert-N species first followed by nitro motifs during the (dis)charging process.

Table S1 Electrochemical metrics of TNB, DB and TA cathodes in Zn batteries.

Sample	Active site	C_m (mAh g^{-1})	Rate (%)	Redox-Site Utilization (%)	Voltage (V)	E (Wh kg^{-1})
TNB	NO_2 + C−N	430	25.3	92.9%	0.90	385
DB	NO_2	92	10.9	14.4%	0.76	70
TA	C−N	109	23.9	89.0%	1.12	122

Table S2 Comparison of capacity (C_m, mAh g^{-1}), energy density (E, Wh kg^{-1}) and cycling life of recently reported aqueous organic batteries in the literatures.

Organic	C_m	E	Life	Refs.
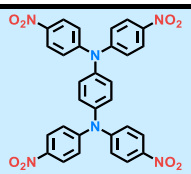 *N*,*N*,*N*′,*N*′-Tetrakis(4-nitrophenyl)-1,4-Benzenediamine (TNB)	430@0.2 A g^{-1} 106@100 A g^{-1}	385	84.1%, 180,000 cycles 10 A g^{-1}	This work
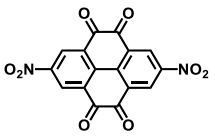 2,7-Dinitropyrene-4,5,9,10-Tetraone (DNPT)	320@0.2 A g^{-1} 113@50 A g^{-1}	226	81.2%, 60,000 cycles 10 A g^{-1}	[S25]
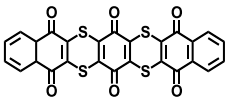 Benzo[b]naphtho[2',3':5,6][1,4]dithiino[2,3-i]thianthrene-5,7,9,14,16,18-hexone (BNDTH)	296@0.05 A g^{-1} 120@10 A g^{-1}	240	65%, 58,000 cycles 10 A g^{-1}	[S26]
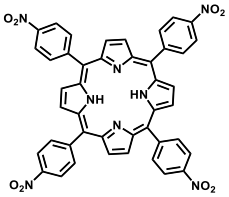 Tetranitroporphyrin (TNP)	338@0.2 A g^{-1} 155@20 A g^{-1}	365	71.6%, 50,000 cycles 10 A g^{-1}	[S27]

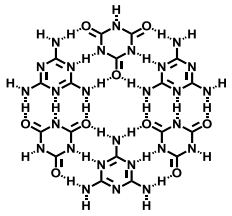 H-Bonded Organic Superstructures (HBOSs)	311@1 A g^{-1} 135@150 A g^{-1}	267	92.3%, 50,000 cycles 10 A g^{-1}	[S28]
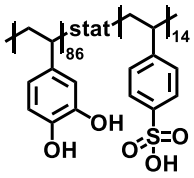 Poly(catechol) ($P(4VC_{86}$-*stat*-$SS_{14})$)	324@0.344 A g^{-1} 98@154.8 A g^{-1}	352	83%, 48,000 cycles 9.4 A g^{-1}	[S29]
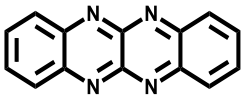 5,6,11,12-Tetraazanaphthacene (TANC)	213@0.1 C 120@20 C	245	71%, 47,500 cycles 10 C	[S30]
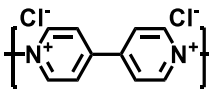 Viologen(bipyridine)-based Organic Framework (VOF)	113@0.25 A g^{-1} 82@20 A g^{-1}	68	70%, 45,000 cycles 5 A g^{-1}	[S31]
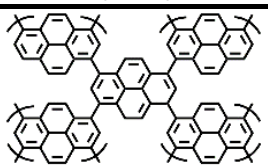 Polypyrene (CLPy)	180@0.05 A g^{-1} 105@3 A g^{-1}	N/A	96.4%, 38,000 cycles 3 A g^{-1}	[S32]
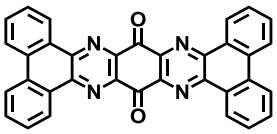 Dibenzo[a,c]dibenzo[5,6:7,8]quinoxalino[2,3-i]phenazine-10,21-dione (TABQ-PQ)	193@0.1 A g^{-1} 140.7@20 A g^{-1}	N/A	90.8%, 30,000 cycles 5 A g^{-1}	[S33]

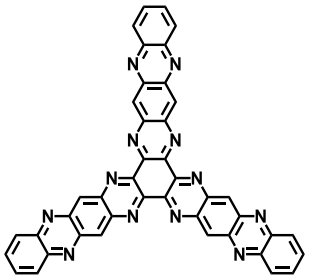 Hexaaz-atrinaphthalene-phenazine (HATN-PNZ)	225@5 A g^{-1} 131@60 A g^{-1}	153.9	92.7%, 30,000 cycles 30 A g^{-1}	[S34]
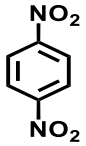 Dinitrobenzene (*p*-DB@CF)	402@0.1 A g^{-1} 214@20 A g^{-1}	230	93.9%, 25,000 cycles 5 A g^{-1}	[S35]
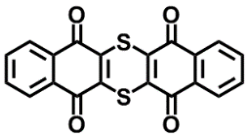 Dibenzo[b,i]thianthrene-5,7,12,14-tetraone (DTT)	211@0.05 A g^{-1} 97@2 A g^{-1}	126.5	83.8%, 23,000 cycles 2 A g^{-1}	[S36]
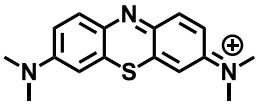 Methylene Blue (MB)	143@0.167 A g^{-1} 58@83.5 A g^{-1}	N/A	86%, 20,000 cycles 16.7 A g^{-1}	[S37]
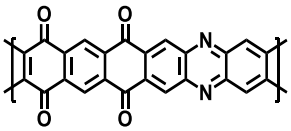 Poly(phenazine-alt-pyromellitic anhydride) (PPPA)	210@0.05 A g^{-1} 140@5 A g^{-1}	N/A	70.6%, 20,000 cycles 5 A g^{-1}	[S38]
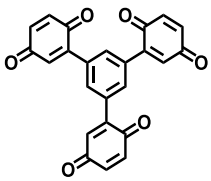 Phenyl Cross-Linked Tri-p-Benzoquinone (Ph-tri-BQ)	402@0.2 A g^{-1} 221@100 A g^{-1}	354	55%, 150,000 cycles 100 A g^{-1}	[S39]

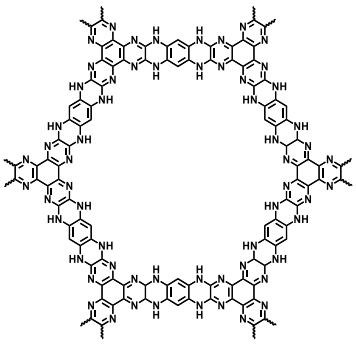 Covalent Organic Framework (HPP-COF)	184.3@5 A g^{-1} 91.7@100 A g^{-1}	N/A	104%, 40,000 cycles 30 A g^{-1}	[S40]
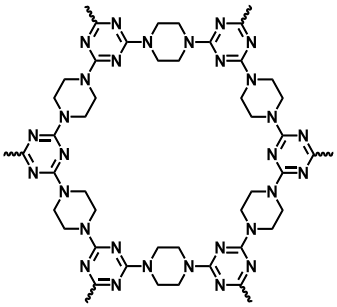 Amphoteric Organic Superstructures (AOSs)	465@0.1 A g^{-1} 151@50 A g^{-1}	412	80.5%, 70,000 cycles 10 A g^{-1}	[S41]
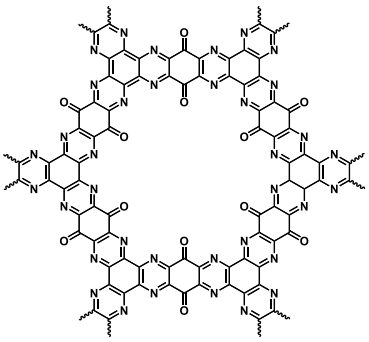 1,4,5,8,9,12-Hexaazatriphenylene-based COF (HAQ-COF)	344@0.1 A g^{-1} 95.6@10 A g^{-1}	N/A	88%, 10,000 cycles 5 A g^{-1}	[S42]
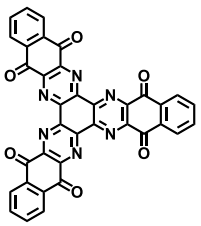 Hexaazatrinaphthalene (BQPH)	429@0.1 A g^{-1} 145@20 A g^{-1}	N/A	82%, 1000 cycles 10 A g^{-1}	[S43]

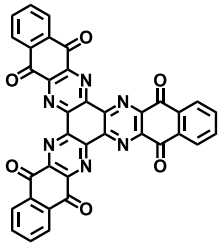 Hexaazatrinaphthalene-quione (HATNQ)	482.5@0.2 A g^{-1} 177.5@9 A g^{-1}	289	75%, 11,000 cycles 5 A g^{-1}	[S44]
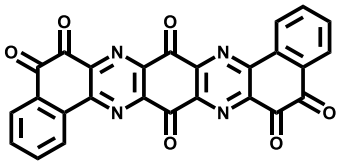 Benzo[a]benzo[7,8]quinoxalino[2,3-i]phenazine-5,6,8,14,15,17-hexane (BBQPH)	498.6@0.2 A g^{-1} 393.6@8 A g^{-1}	355	95%, 1000 cycles 5 A g^{-1}	[S45]
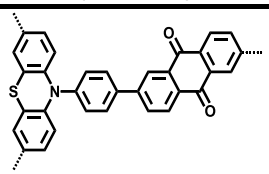 Donor-Acceptor Polymers (PPTZ-AQ)	205@0.05 A g^{-1} 165@2 A g^{-1}	N/A	78.4%, 60000 cycles 5 A g^{-1}	[S46]
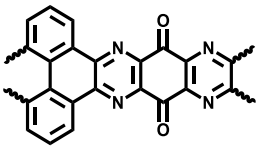 Poly(4,5-dihydrophenanthro[4,5-abc]pyrazino[2,3-i]phenazine-10,15-dione) (PYTQ-CNT)	295@0.1 A g^{-1} 85@2 A g^{-1}	413	74.6%, 4000 cycles 1 A g^{-1}	[S47]
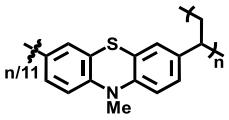 Poly(3-vinyl-N-methylphenothiazine) (X-PVMPT)	167@0.5 C 64@100 C	355	88%, 5000 cycles 10 C	[S48]
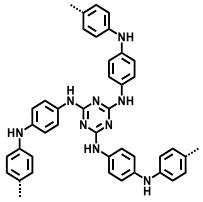 Cross-Linked Polyaniline (C-PANI)	209@5 A g^{-1} 133@25 A g^{-1}	N/A	91.7%, 39000 cycles 25 A g^{-1}	[S49]

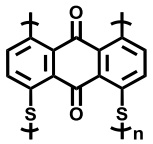 Anthraquinone-based Carbonyl Polymers (*d*-PAQS)	216@0.2 C 106@10 C	N/A	95%, 1000 cycles 10 C	[S50]
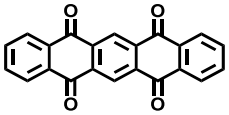 5,7,12,14-Pentacenetetrone (PT)	150.5@5 A g^{-1} 86.1@100 A g^{-1}	200.4	114%, 3000 cycles 30 A g^{-1}	[S51]
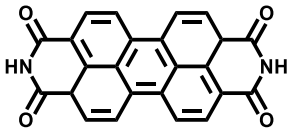 3,4,9,10-Perylenetetracarboxylic Diimide (PTCDI)	131.8@0.1 A g^{-1} 86.2@10 A g^{-1}	N/A	72.7%, 68000 cycles 1 A g^{-1}	[S52]
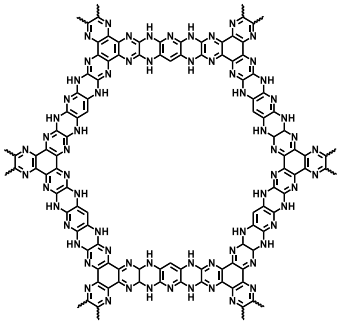 (PTHAT-COF)	155.5@1 A g^{-1} 60@20 A g^{-1}	159.7	83.6%, 10000 cycles 10 A g^{-1}	[S53]
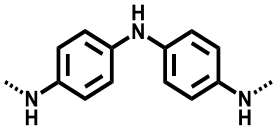 Polyaniline (PANI)	0.3@2 mA cm^{-2} 0.15@20 mA cm^{-2}	N/A	82.7%, 1600 cycles 20 mA cm^{-2}	[S54]

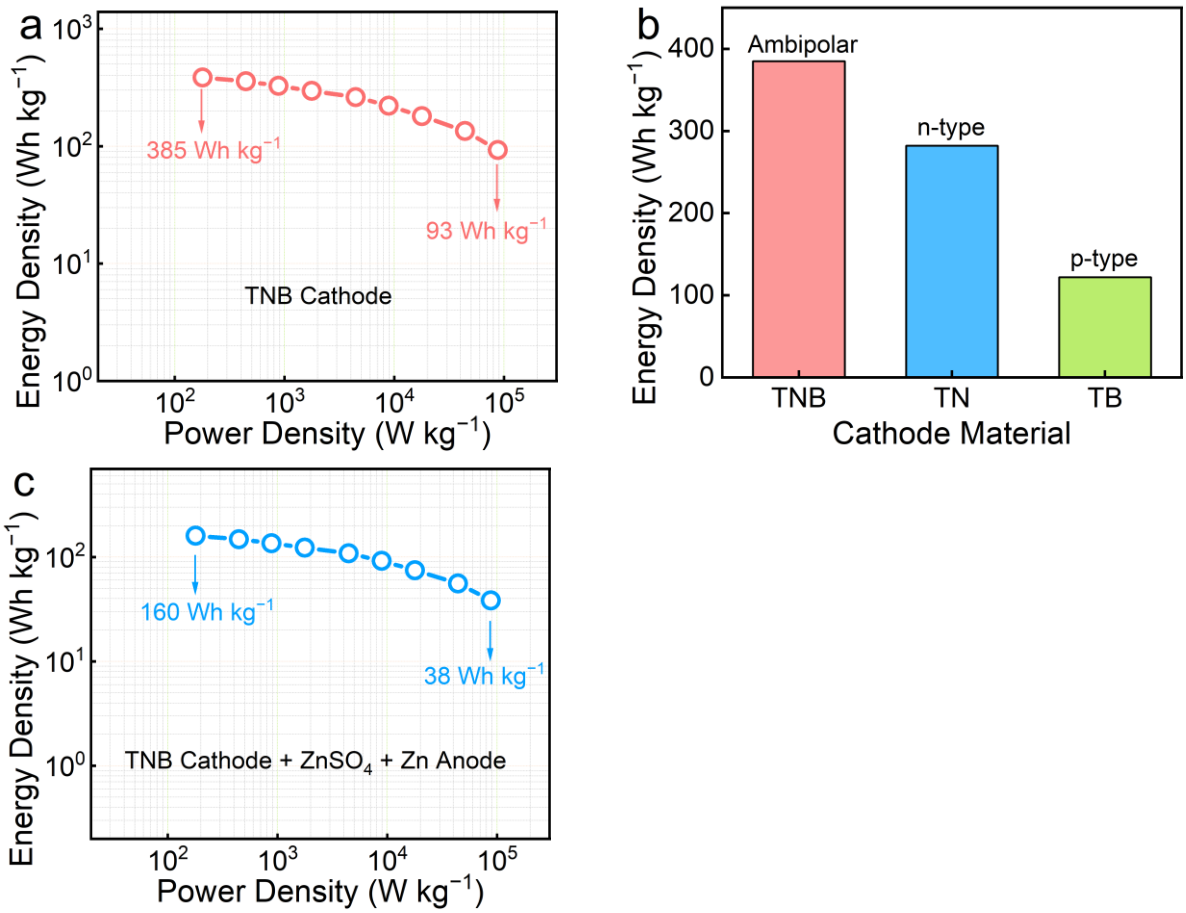

Fig. S15 (a) Ragone plots of Zn||TNB battery based on the mass loading of TNB in the cathode (3.5 mg cm^{-2}) using 3 M $ZnSO_4/H_2O$ electrolyte. (b) Comparison of energy density of three ZOBs based on different organic cathodes. (c) Battery-level energy density of Zn||TNB battery.

Notes: The average discharge voltage (0.90 V) is calculated by dividing the energy density (385 Wh kg^{-1}) by the corresponding discharge capacity (430 mAh g^{-1}, Fig. 2a).

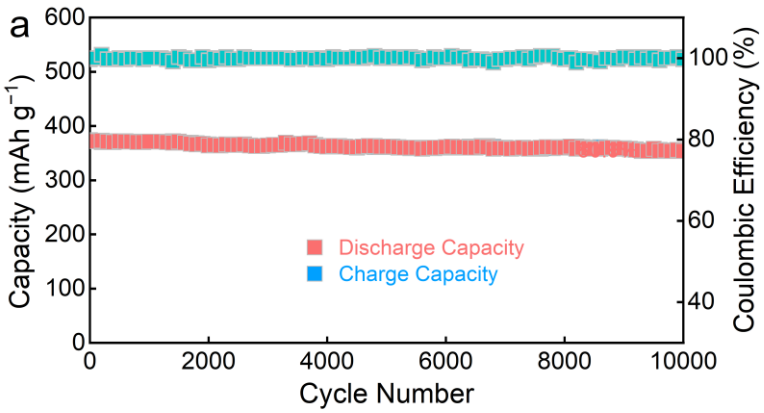

Fig. S16 Cycling stability of Zn||TNB battery at 1 A g^{-1}.

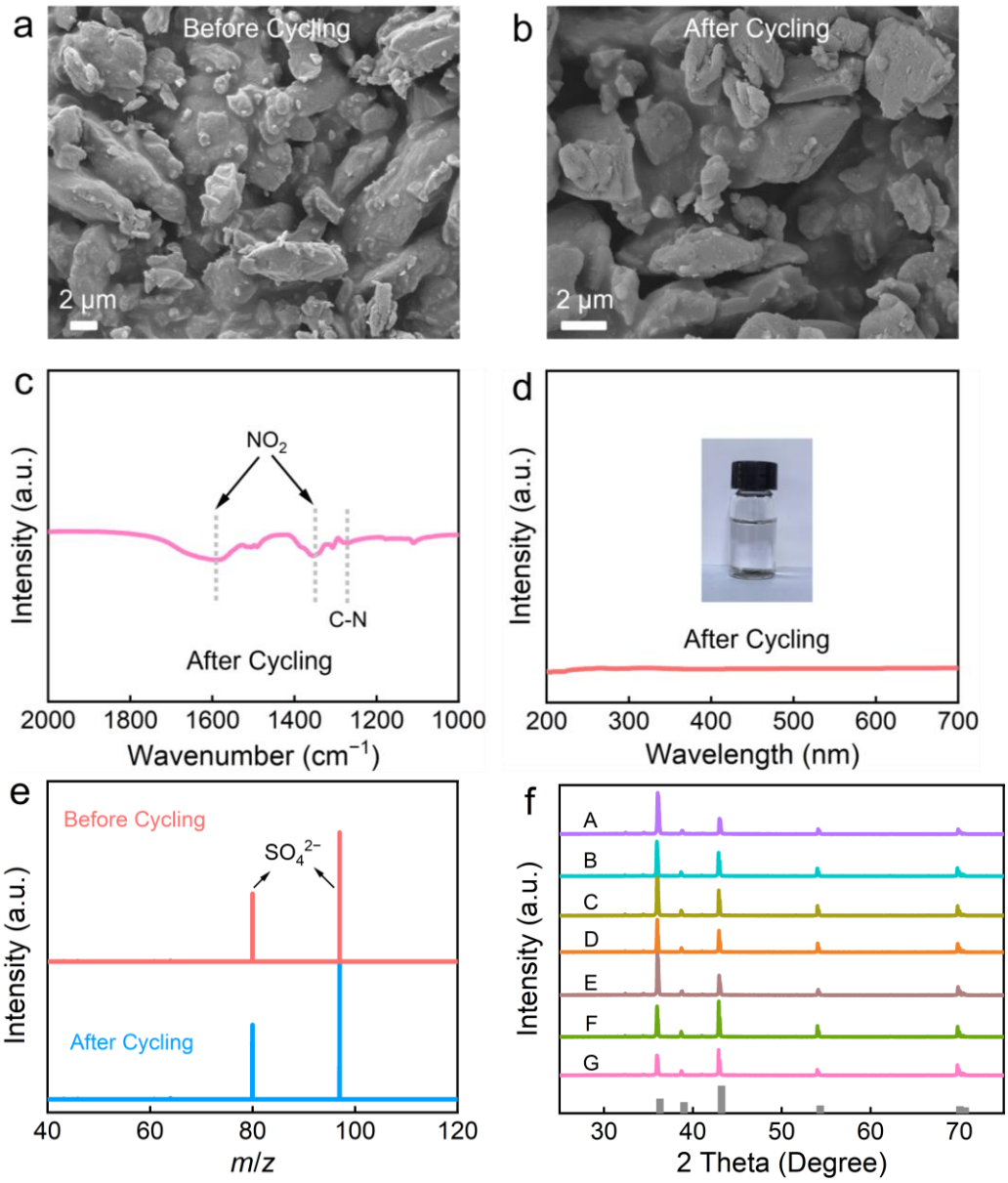

Fig. S17 (a, b) SEM images of TNB cathode before and after long-term cycling. (c) FT-IR spectrum, (d) UV-Vis spectrum and digital photograph of cycled TNB cathode in 3 M $ZnSO_4/H_2O$ electrolyte. (e) Liquid Chromatography-Mass Spectrometry (LC-MS) analysis of $ZnSO_4/H_2O$ soaked with TNB cathode before and after cycling. (f) *Ex-situ* XRD patterns of Zn anodes at seven (dis)charged markers.

Notes: SEM images indicate that there is no structural destruction for TNB (Fig. S17a and b). FT-IR spectra of TNB cathode after cycling still shows strong redox signals of nitro/tert-N groups (Fig. S17c). No UV-Vis absorption signals after cycling suggest the anti-dissolution effect of TNB cathode (Fig. S17d). These results confirm the structural and functional robustness of TNB cathode without causing capacity degradation. LC-MS was

applied to detect the dissolved redox-active species of TNB cathode in 3 M $ZnSO_4/H_2O$ electrolyte. The chromatographic peaks of post-cycling $ZnSO_4/H_2O$ electrolyte are the same as before cycling (Fig. S17e), without extra impure peaks of dissolved redox-active functional species, indicating that TNB is insoluble during cycling. Zn anode shows consistent XRD patterns at seven (dis)charged markers (Fig. S17f), indicating its desirable structural stability and high compatibility with TNB cathode for propelling efficient redox reactions.

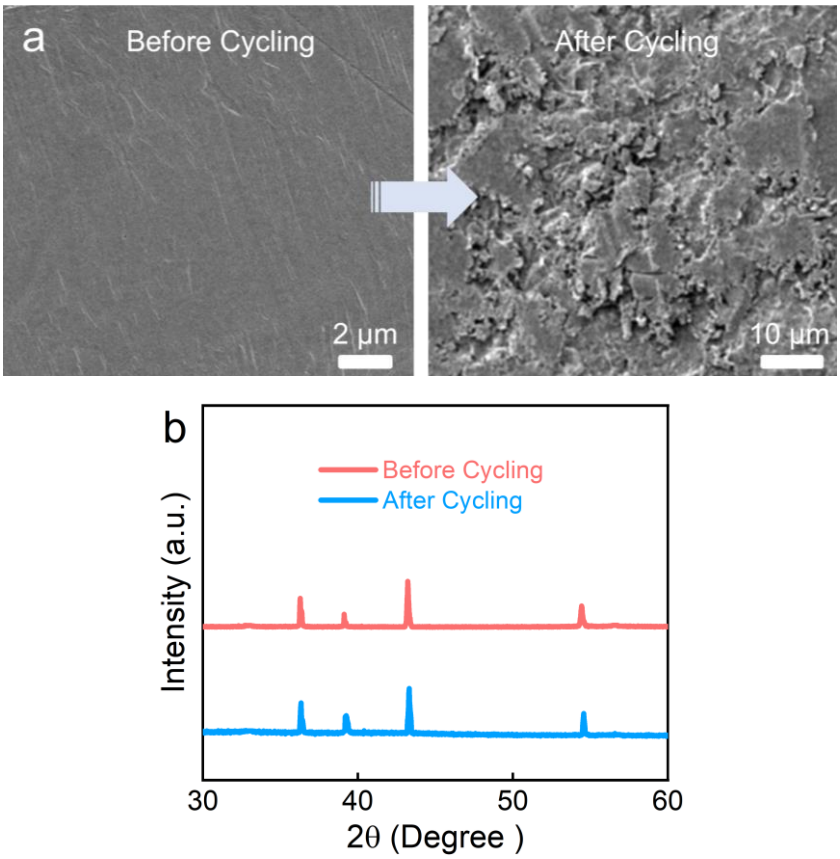

Fig. S18 (a) SEM images and (b) XRD patterns of Zn anode before and after long-term cycling.

Notes: Compared with pristine Zn foil, the Zn anode shows rough surface geometries, which derives from the repeat plating/stripping reaction of Zn anode during long-term (dis)charged cycling processes. The high structural stability and exceptional anti-dissolution of nonplanar TNB cathode in $ZnSO_4/H_2O$ electrolyte (Fig. S17) contribute to the long-term cycling behavior of Zn||TNB battery (Fig. 2f). Of note, Zn||TNB battery delivers a superb cycling lifespan of 180,000 cycles, albeit with a 15.9% capacity loss.

This is because the repeated plating/stripping reaction of the Zn anode during long-term cycling induces structural degradation with disordered surface morphologies (Fig. S18), which is the main limitation for the persistent operation of Zn||TNB cell.

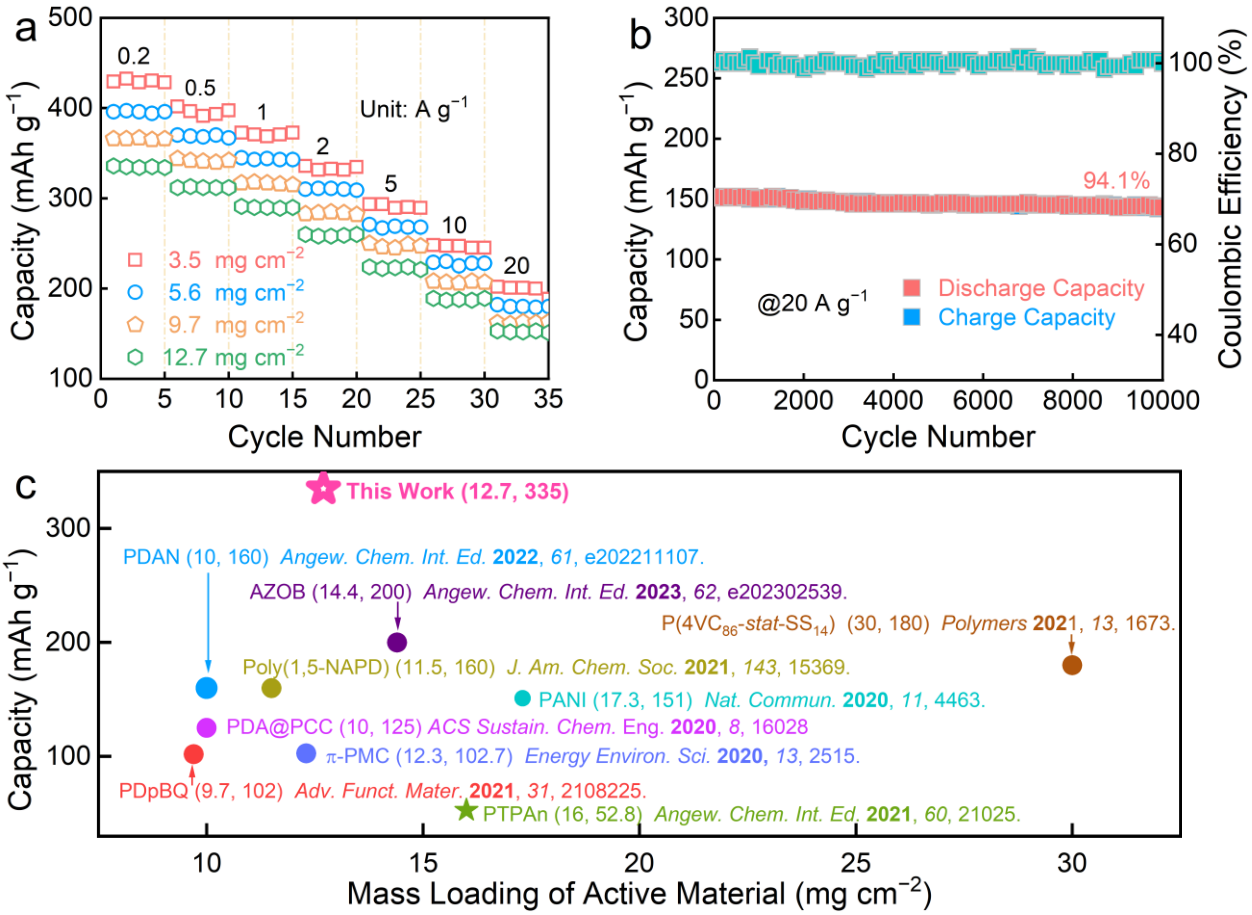

Fig. S19 Electrochemical performances of Zn||TNB battery at the practical-level mass loading of 12.7 mg cm^{-2} for TNB in the cathode. (a) Rate performances of TNB cathode with different mass loadings. (b) Cycling stability. (c) Capacity comparison with reported organic cathode materials. Note: (*x*, *y*) = (mass loading, specific capacity).

Table S3 Cycling performance of practical-level mass-loading TNB cathode compared with reported organics materials in the literature.

Organic Material	Mass Loading	Cycling Life	Reference
TNB	12.7 mg cm^{-2}	94.1%, 10000 cycles	This work
PZ-2OH	14.8 mg cm^{-2}	80%, 500 cycles	*Energy Environ. Sci.* **2024**, *17*, 114−122.
PI-1/CNT	12.5 mg cm^{-2}	90%, 500 cycles	*Adv. Mater.* **2022**, *34*, 2200077.
TMBQ@KMCN	10.6 mg cm^{-2}	100%, 850 cycles	*Energy Environ. Sci.* **2024**, *17*, 5162−5172.
PDAN	10.0 mg cm^{-2}	94%, 1000 cycles	*Angew. Chem. Int. Ed.* **2022**, *61*, e202211107.
PTL	6.27 mg cm^{-2}	98%, 100 cycles	*Angew. Chem. Int. Ed.* **2025**, *64*, e202425082.
MBTS	6.7 mg cm^{-2}	96.4%, 200 cycles	*J. Am. Chem. Soc.* **2025,** *147*, 5089−5098.
DPT	5.0 mg cm^{-2}	93%, 450 cycles	*J. Am. Chem. Soc.* **2023**, *145*, 25604−25613.

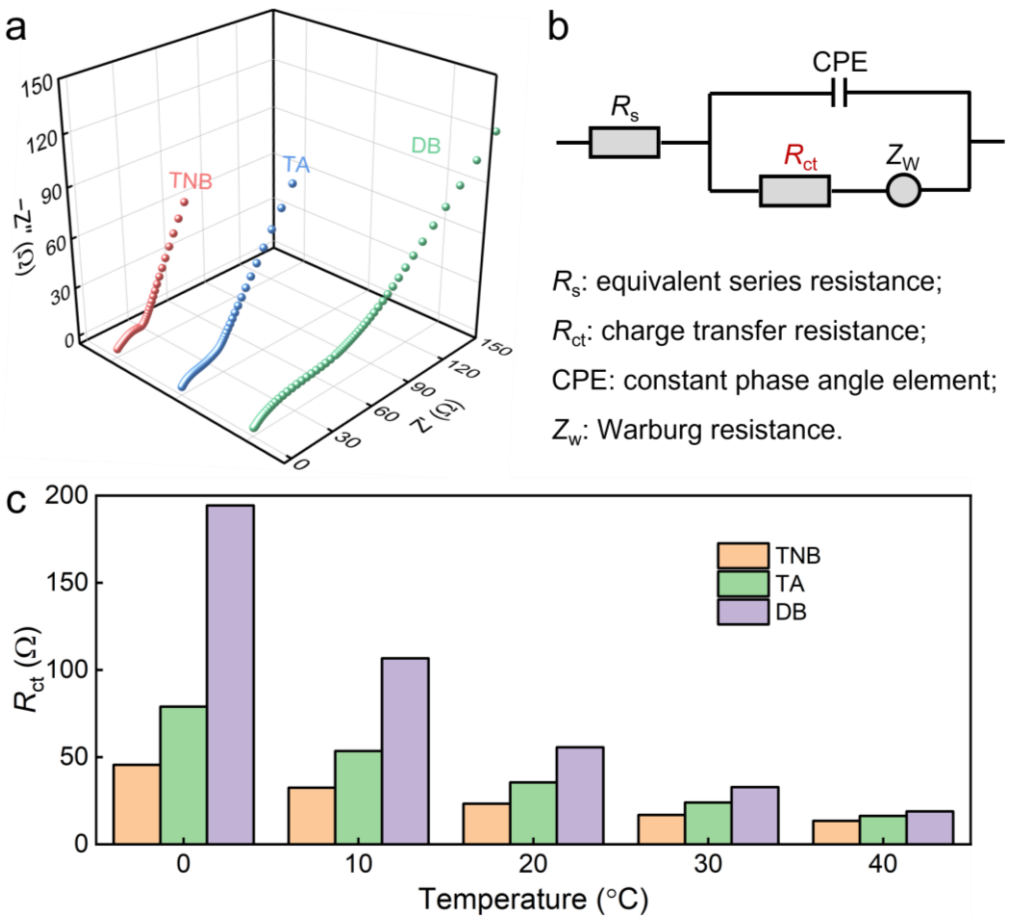

Fig. S20 (a) EIS profiles of TNB, TA and DB cathodes in Zn batteries using aqueous $ZnSO_4$ electrolyte. (b) The adopted equivalent circuit for fitting the Nyquist plots. (c) Calculated R_{ct} values at different temperatures.

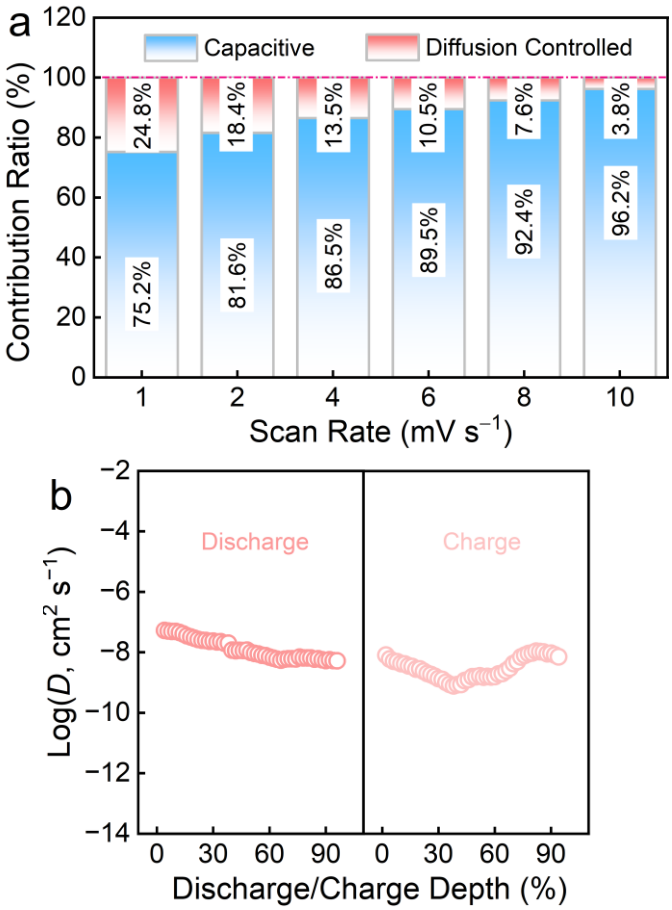

Fig. S21 (a) Capacitive contribution ratios of Zn||TNB battery. (b) Calculated *D* values of TNB cathode.

Notes: CV profiles show three pairs of redox signals, which are indicative of a three-step electrochemical process between charge carriers and TNB cathode. Plotting log*i* against log*v* yields high power-exponent b values of 0.93−0.99 for the six redox peaks. It is well-established that a b-value is close to 0.5 denotes a diffusion-controlled process, while a b-value is close to 1 signifies a capacitive-controlled process in the charge storage mechanism. Organic materials with high b values close to 1 were often classified as pseudocapacitance-type materials.[S55] This suggests pseudocapacitance-dominated chemistry behavior of TNB, endowing Zn||TNB battery with rapid surface charge-storage kinetics and superior electrochemical performances.

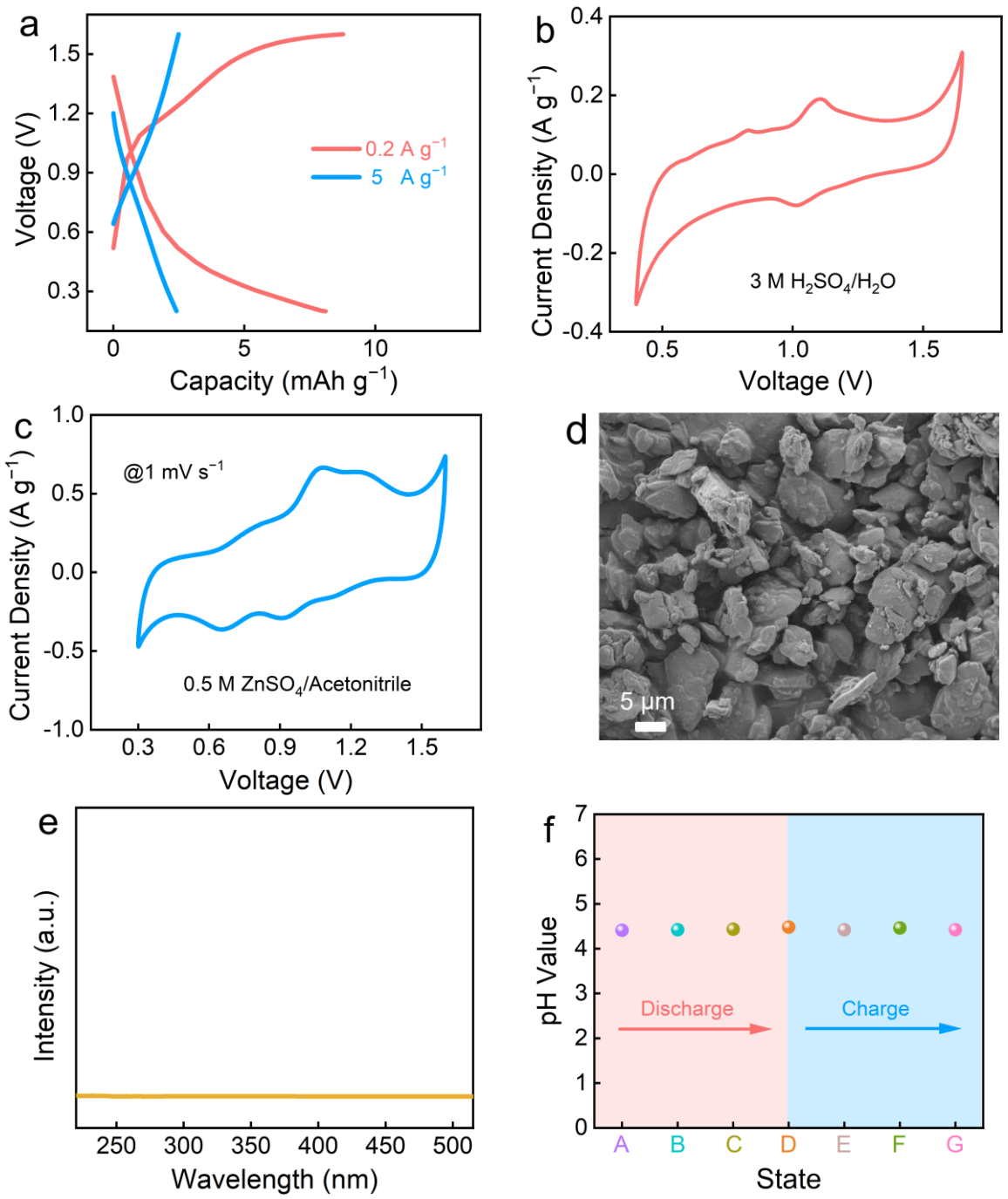

Fig. S22 (a) A GCD curve of Zn||TNB battery using H_2SO_4/H_2O electrolyte (with the same pH value of $ZnSO_4/H_2O$ electrolyte) at 0.2 and 5 A g^{-1}. (b) CV curve of Zn||TNB battery using 3 M H_2SO_4/H_2O electrolyte at 1 mV s^{-1}. (c) CV curve of Zn||TNB battery using 0.5 M $ZnSO_4$/acetonitrile electrolyte at 1 mV s^{-1}. (d) A SEM image of TNB cathode at the fully discharged state. (e) UV-Vis spectrum of $ZnSO_4/H_2O$ electrolyte immersed with TNB cathode. (f) Local pH fluctuations of TNB cathode at different electrochemical states.

Notes: Compared with 3 M $ZnSO_4/H_2O$ electrolyte (pH≈4.4), Zn||TNB battery using H_2SO_4/H_2O electrolyte displays completely different electrochemical behaviors with

negligible capacity contribution (8 mAh g^{-1} at 0.2 A g^{-1}, Fig. S22a). Despite the smaller and faster size and kinetics of H^+ compared to Zn^{2+}, an extremely low capacity of 2 mAh g^{-1} still can be observed at a high current density of 5 A g^{-1}. These results indicate that H^+ ion does not participate in the electrochemical reaction process of Zn||TNB battery. The slight acidity and extremely low anion concentration of H_2SO_4/H_2O electrolyte (pH≈4.4) fail to effectively activate the redox activity of p-type amine groups, leading to insignificant capacity storage. Furthermore, CV curve of TNB cathode using 3 M H_2SO_4/H_2O electrolyte shows a pair of oxidation-reduction peaks at the high-potential region (Fig. S22b), which closely resemble those observed in 3 M $ZnSO_4/H_2O$ electrolyte. However, it exhibits a low H^+-storage capacity of 70 mAh g^{-1} even at the high-H^+-concentration electrolyte, indicating that the limited charge storage is dominated by the p-type redox reaction of tert-N species. When operated in 0.5 M $ZnSO_4$/acetonitrile electrolyte, CV curve of TNB cathode shows the same three pairs of redox peaks (Fig. S22c) as those observed in 3 M $ZnSO_4/H_2O$ electrolyte. Meanwhile, its capacity is also almost identical to that in 3 M $ZnSO_4/H_2O$ electrolyte, manifesting the strong Zn^{2+}/SO_4^{2-} co-storage activity of TNB cathode. Note that H^+ storage is a common phenomenon that prevails in aqueous ZOBs. H^+ involvement as the charge carrier changes the local pH value to generate OH^- ions, which subsequently precipitates Zn^{2+} and SO_4^{2-} to form $Zn_4SO_4(OH)_6{\cdot}xH_2O$ nanoflakes on the cathode surface.[S55] In our Zn||TNB battery system, the exclusion of H^+ charge carrier is also reflected by the absence of flaky Zn precipitation byproducts on the surface of TNB cathode at the fully discharged state (Fig. S22d), revealing the negligible role of H^+ during the operation of Zn||TNB battery. There is no UV-Vis absorption signal for fully reduced TNB cathode in $ZnSO_4/H_2O$ electrolyte (Fig. S22e), indicating its robust structure during the electrochemical reaction process. To observe the local pH fluctuations of TNB cathode at different (dis)charged states, *in-situ* pH test was conducted by placing a direct-reading pH meter in a constructed two-electrode Zn||TNB system with 3 M $ZnSO_4/H_2O$ electrolyte. Of note, the glass electrode of the pH meter is attached to the surface of TNB cathode to monitor the most reliable pH response. The local pH value is generally constant during the discharge/charge process (Fig. S22f), excluding the possibility of proton involvement in TNB.

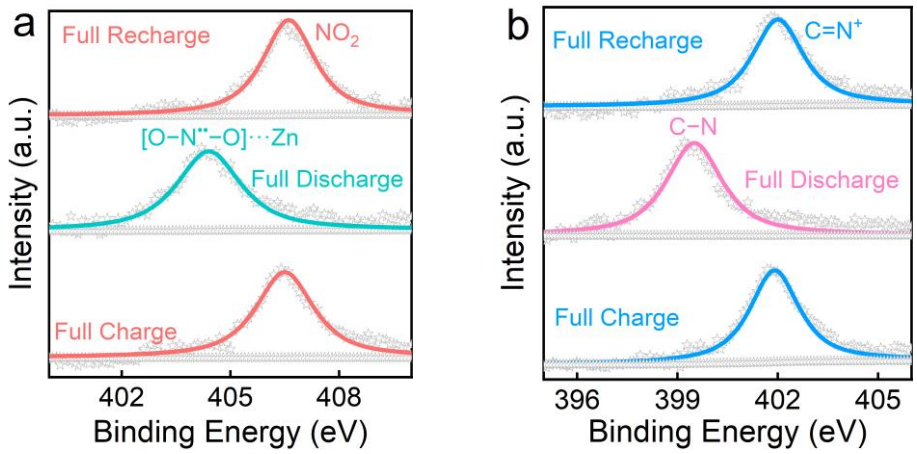

Fig. S23 *Ex-situ* high-resolution N 1s spectra of (a) DB cathode and (b) TA cathode at different discharge/charge states.

Notes: During the electrochemical process, the nitro groups of DB cathode show the reversible attenuation/enhancement variation trend, elucidating their high redox activity (Fig. S23a). Of note, a new peak can be observed at the full discharge state, which can be attributed to the formation of nitro intermediates ([O−N••−O]···Zn). These results interpret the n-type redox reaction between Zn^{2+} cations and NO_2 groups in DB cathode. Moreover, with the proceeding of the charging, $C=N^+$ signal appears in TA cathode accompanied by the vanishing of C−N species (Fig. S23b), confirming the anionic SO_4^{2-}-doping reaction. Such variations agree with the N 1s XPS spectra results of TNB cathode (Fig. 3c), involving the formation of [O−N••−O]···Zn species during discharging and $C=N^+$ species during charging. All these results confirm the alternative storage of opposite charges (Zn^{2+} and SO_4^{2-}) in bipolar multisite motifs (nitro and tert-N) of TNB scaffold.

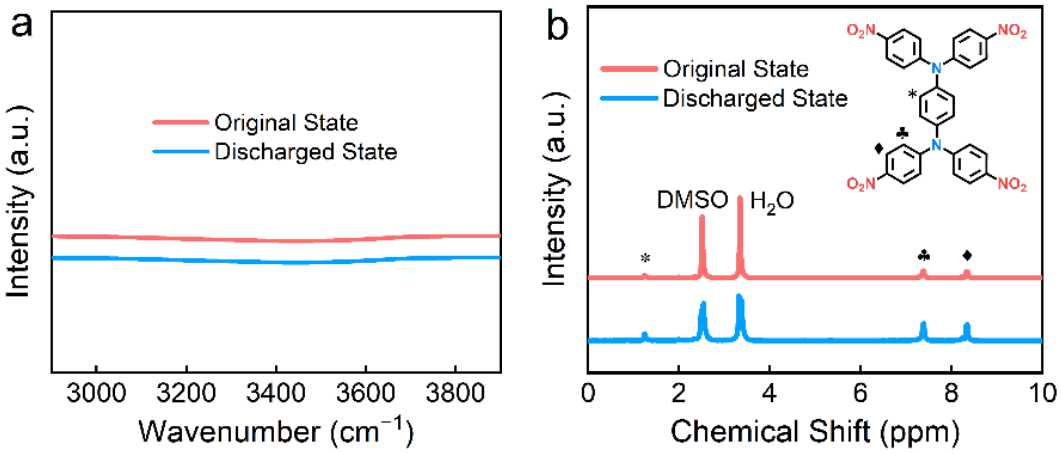

Fig. S24 (a) FT-IR spectra and (b) ^{1}H NMR spectra of TNB cathode at different electrochemical states.

Notes: FT-IR and ^{1}H NMR spectrum characterizations were performed to track the evolution of nitro groups in TNB cathode during the reduction process (Fig. S24). Generally, H^+-driven six-electron transfer per nitro group in nitroarene reduction is accompanied by the generation of amino compounds during the first discharge in acidic electrolytes, showing irreversible nitro conversion for subsequent redox reactions.[S57] Of note, there is no obvious signal of hydroxylamine/amine species in FT-IR spectra at 3000~3500 cm^{-1} for reduced TNB cathode (Fig. S24a). Meanwhile, ^{1}H NMR spectra show identical signals before and after reduction reaction (Fig. S24b), suggesting the unchanged H atom environments of TNB cathode. These results imply that $-NO_2$ groups of TNB cathode are not converted to $-NH_2$ groups in H^+-containing $ZnSO_4/H_2O$ electrolyte (pH≈4.4). Evidently, comprehensive characterizations including electrochemical results (Fig. 2a−c), *ex-situ* FT-IR spectra (Fig. 3b), and *ex-situ* XPS spectra (Fig. 3d−f) elucidate that nitro groups propel highly reversible Zn^{2+} (de)coordination redox reactions (excluding H^+ involvement, Fig. S22) based on electrochemical rearrangements of chemical bonds. This devotes to reversible and stable multi-electron charge storage of TNB cathode for advanced ZOBs (Table S2).

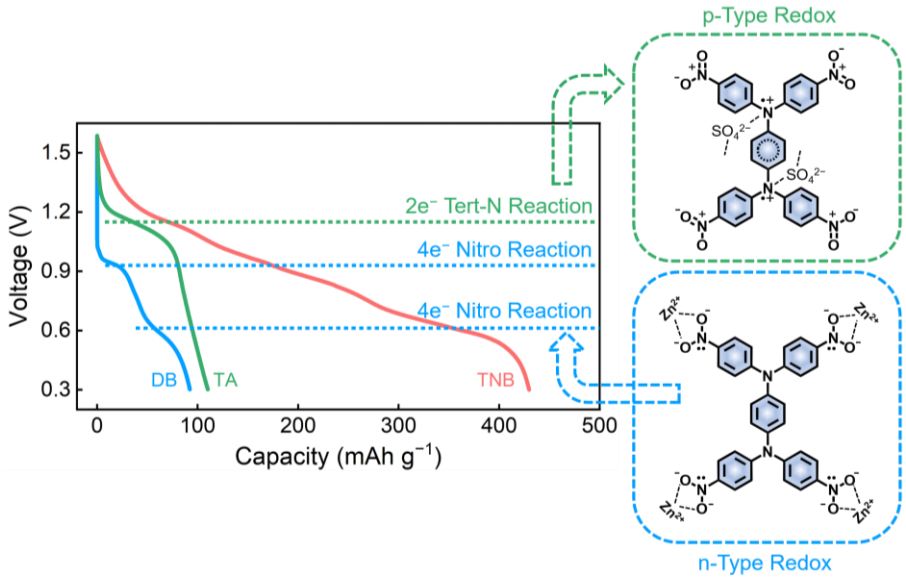

Fig. S25 GCD curves of TNB, TA and DB cathodes in ZOBs.

Notes: To further reveal the reaction process of TNB cathode during the electrochemical process, control electrochemical experiments for DB (only involving n-type nitro groups) and TA (only involving p-type tert-N groups) cathodes were performed in 3 M $ZnSO_4/H_2O$ electrolyte. A redox platform (1.12 V) is detected for Zn||TA battery, which conforms to Zn||TNB battery, suggesting that TNB can accommodate SO_4^{2-} anions. Furthermore, two redox signals (0.93/0.62 V) of the GCD curve of Zn||DB battery overlaps with that of Zn||TNB battery. This means two-step successive Zn^{2+} coordination with TNB. These results indicate that SO_4^{2-} anions and Zn^{2+} cations dominate the energy storage of TNB cathode by the stepwise redox reaction with tert-N species first followed by nitro motifs during the (dis)charging process.

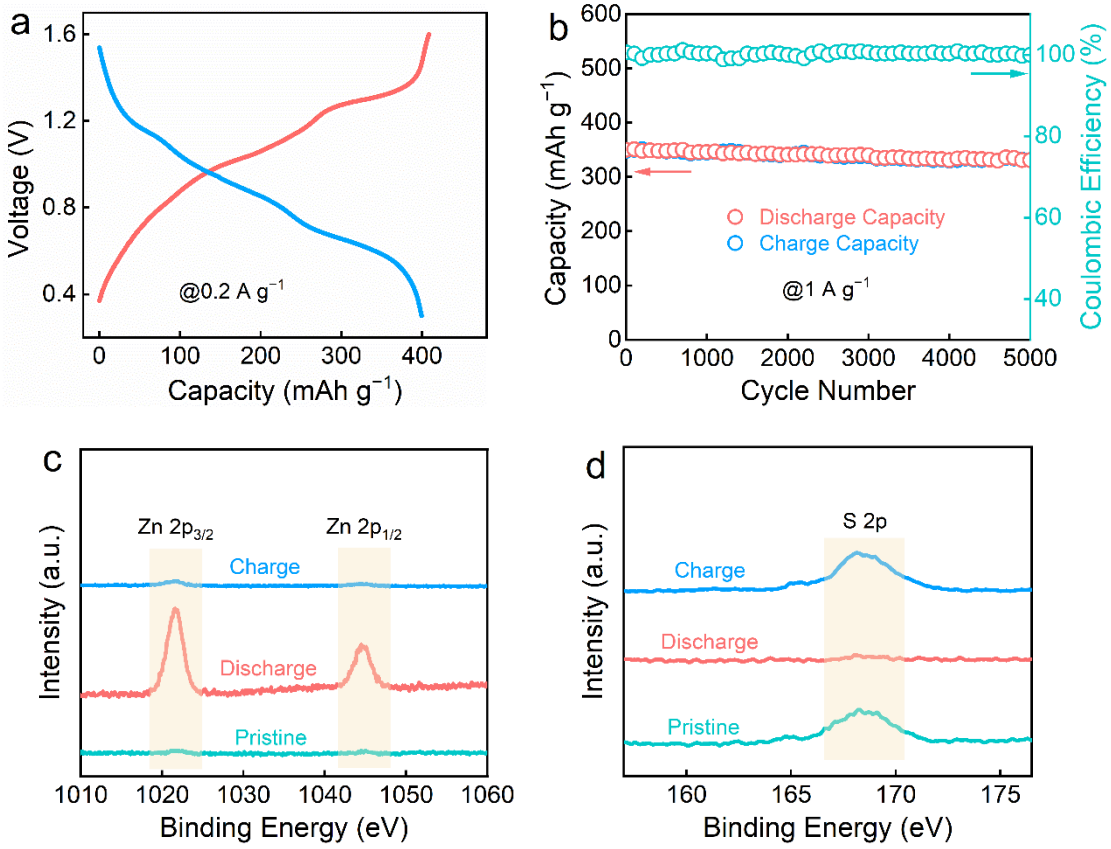

Fig. S26 (a) GCD profile and (b) cycling capacity of TNB cathode. *Ex-situ* XPS spectra of (c) Zn 2p and (d) S 2p of TNB cathode at different electrochemical states.

Notes: For comparison, the electrochemical properties of TNB cathode were also evaluated in 1 M $ZnSO_4/H_2O$ electrolyte (Fig. S26). GCD profile of TNB cathode in this electrolyte (Fig. S26a) exhibits redox behavior similar to that observed in 3 M $ZnSO_4/H_2O$ electrolyte (Fig. 2a), confirming a three-step redox charge storage process. TNB cathode in 1 M $ZnSO_4/H_2O$ electrolyte delivers comparable but slightly reduced capacity storage (Fig. S26b) relative to that in 3 M $ZnSO_4/H_2O$ electrolyte (Fig. S16a). To gain mechanistic insight of the co-storage of Zn^{2+} cations and SO_4^{2-} anions, *ex-situ* XPS analysis was performed by monitoring Zn 2p and S 2p signals during (dis)charging (Fig. S26c and d). The Zn 2p signal increases upon discharge and decreases after charge, confirming the reversible storage of Zn^{2+} ions in TNB cathode (Fig. S26c). In contrast, the S 2p signal shows a marked decrease after discharge and returns to its initial state upon recharging, indicating reversible (de)coordination of SO_4^{2-} anions (Fig. S26d). These results suggest that the Zn^{2+}/SO_4^{2-} co-storage mechanism remains adapted for TNB cathode in 1 M $ZnSO_4/H_2O$ electrolyte.

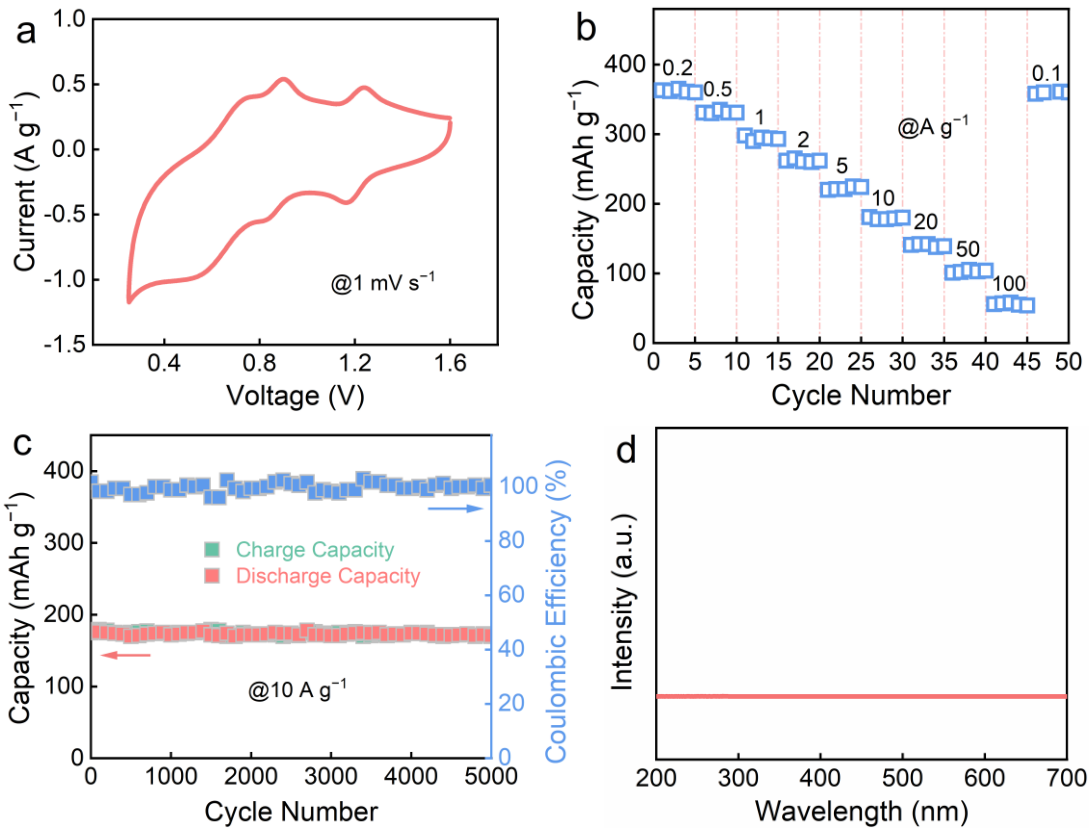

Fig. S27 Electrochemical properties of TNB cathode in aqueous $NiSO_4$ electrolyte. (a) CV profile. (b) Rate capacities. (c) Cycling stability. (d) UV-Vis spectrum of $NiSO_4/H_2O$ electrolyte immersed with TNB cathode.

Notes: CV profile of TNB cathode in aqueous $NiSO_4$ electrolyte shows three pairs of redox peaks (Fig. S27a), indicating a continuous three-step redox process that is consistent with that observed in aqueous $ZnSO_4$ electrolyte. This result suggests that Ni^{2+} cations participate in the charge storage alongside SO_4^{2-} anions. Furthermore, TNB cathode delivers high electrochemical capacities across various current densities (Fig. S27b), demonstrating good rate capability in aqueous $NiSO_4$ electrolyte. Notably, it also maintains stable capacities over 5000 cycles at 10 A g^{-1} (Fig. S27c), reflecting the intrinsic structural stability of TNB material. UV-vis spectra of TNB cathode after long-term cycling (Fig. S27d) further confirm its structural robustness and anti-dissociation ability in aqueous $NiSO_4$ electrolyte, which underpins the durable operation of Zn||TNB battery. Collectively, these results confirm that the proposed ambipolar redox mechanism is not specific to Zn^{2+}; rather, Ni^{2+} can also participate in reversible cation storage. This highlights the broad electrochemical compatibility of TNB cathode with different cations and supports its efficient performance in ZOBs.

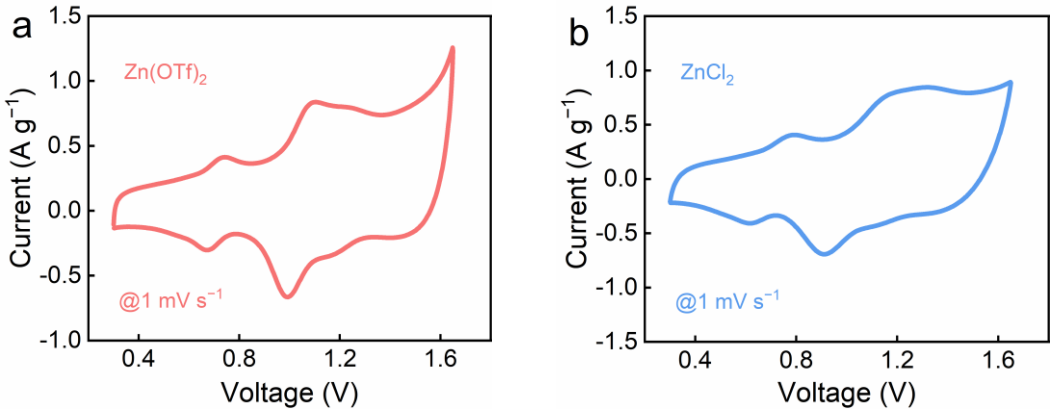

Fig. S28 CV profiles of TNB cathode in aqueous (a) $Zn(OTf)_2$ and (b) $ZnCl_2$ electrolytes.

Notes: CV profiles of TNB cathode in both aqueous $Zn(OTf)_2$ and $ZnCl_2$ electrolytes show desirable charge storage capacity with three pairs of redox peaks, suggesting the existence of a continuous three-step redox reaction behavior. This feature is well consistent with those in aqueous $ZnSO_4$ electrolyte, indicating the cation/anion co-storage redox mechanism. These results confirm that the proposed cation/anion co-storage redox mechanism is not anion-specific and highlight the broad electrochemical compatibility of TNB cathode with Zn anode across different aqueous electrolytes, promoting the efficient electrochemical performance of ZOBs.

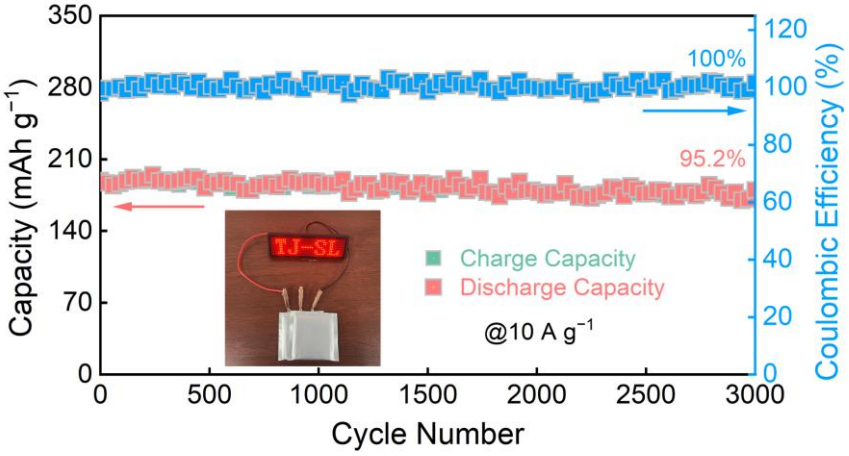

Fig. S29 Cycling stability of Zn||TNB pouch battery with the mass loading of 12.5 mg cm^{-2}_{TNB}.

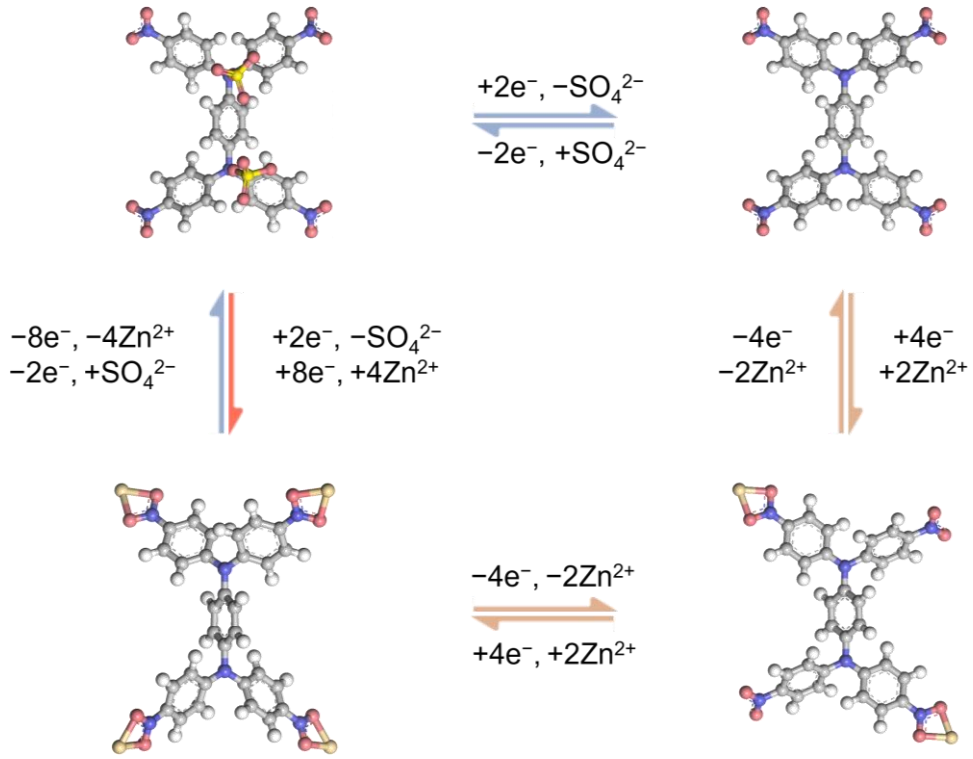

Fig. S30 The optimized reaction sequence and organic-ion coordination structures.

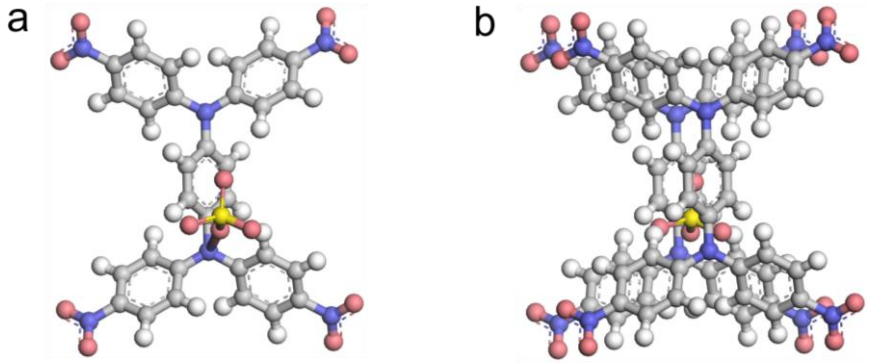

Fig. S31 Theoretical calculation-optimized molecular structures of (a) one TNB molecule coordinated with a SO_4^{2-} anion and (b) two TNB molecules coordinated with a SO_4^{2-} anion.

Notes: The binding energy (ΔE) demanded for a SO_4^{2-} anion to combine with two tert-N sites of TNB is −3.68 eV (Fig. S29), which is lower than that of −4.06 eV required for two TNB molecules coordinated with a SO_4^{2-} anion. Such a result indicates the favorable SO_4^{2-}-binding environment of nonplanar π-π stacked sandwich structure, which does a favor to stable multielectron redox charge storage process of TNB cathode in ZOBs.

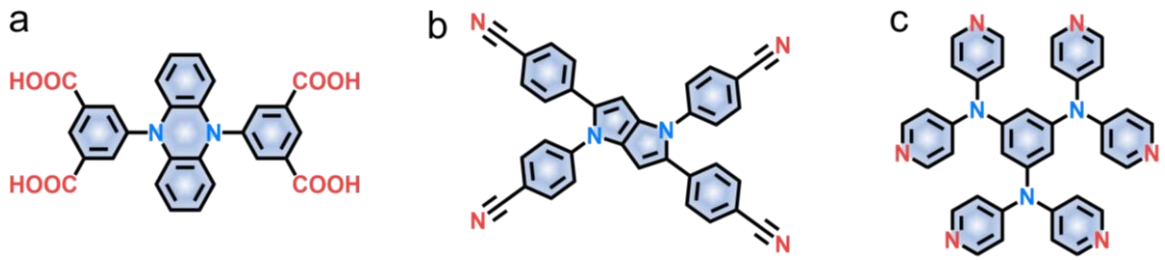

Fig. S32 Molecular structures of (a) PNA, (b) PPT, and (c) HBT.

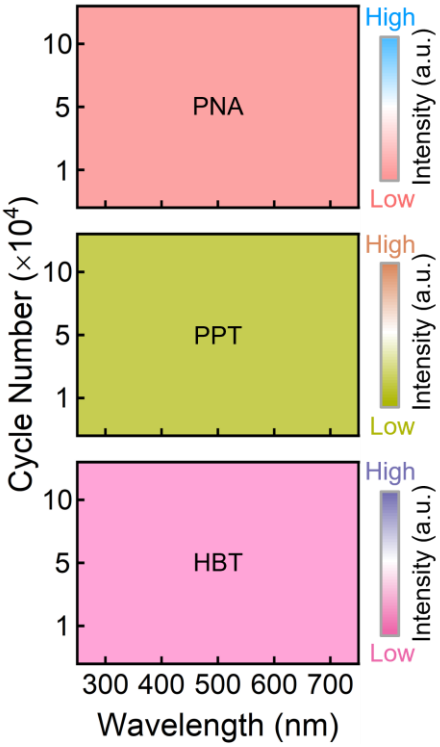

Fig. S33 UV-vis spectra of aqueous $ZnSO_4$ electrolytes immersed with cycled PNA, PPT, and HBT cathodes, respectively.

Section S5. References

[S1] M. J. Frisch, G. W. Trucks, H. B. Schlegel, et al., Gaussian 16 Revision. A.03, Gaussian Inc., Wallingford, CT, **2016**.

[S2] E. R. Johnson, S. Keinan, P. Mori-Sánchez, J. Contreras-García, A. J. Cohen, W. Yang, *J. Am. Chem. Soc.* **2010**, *132*, 6498.

[S3] T. Lu, F. Chen, *J. Comput. Chem.* **2012**, *33*, 580.

[S4] W. Humphrey, A. Dalke, K. Schulten, *J. Mol. Graph.* **1996**, *14*, 33.

[S5] L. Martínez, R. Andrade, E. G. Birgin, J. M. Martínez, *J. Comput. Chem.* **2009**, *30*, 2157.

[S6] M. J. Abraham, T. Murtola, R. Schulz, S. Páll, J. C. Smith, B. Hess, E. Lindahl, *SoftwareX*. **2015**, *6*, 19.

[S7] G. Henkelman, A. Arnaldsson, H. Jónsson, Comput. *Mater. Sci.* **2006**, *36*, 354.

[S8] S. Pronk, S. Páll, R. Schulz, P. Larsson, *Bioinformatics* **2013**, *29*, 845.

[S9] B. Hess, C. Kutzner, D. van der Spoel, E. Lindahl, *J. Chem. Theor. Comput.* **2008**, *4*, 435.

[S10] W. L. Jorgensen, D. S. Maxwell, J. Tirada-Rives, *J. Am. Chem. Soc*. **1996**, *118*, 11225.

[S11] H. J. C. Berendsen, J. R. Grigera, T. P. Straatsma. *J. Phys. Chem.* **1987**, *91*, 6269.

[S12] B. Hess, H. Bekker, H. J. C. Berendsen and J. G. E. M. Fraaije, *J. Comput. Chem.* **1997**, *18*, 1463.

[S13] G. Bussi, D. Donadio, M. Parrinello, *J. Phys. Chem.* **2007**, *126*, 014101.

[S14] U. Essmann, L. Perera, M.L. Berkowitz, T. Darden, H. Lee, L.G. Pedersen, *J. Phys. Chem.* 1995, **103**, 8577.

[S15] W. Kohn, L. J. Sham, *Phys. Rev.* **1965**, *140*, A1133.

[S16] G. Kresse, J. Furthmüller, *Comp. Mater. Sci.* **1996**, *6*, 15.

[S17] P. E. Blöchl, *Phys. Rev. B* **1994**, *50*, 17953.

[S18] J. P. Perdew, J. A. Chevary, S. H. Vosko, K. A. Jackson, M. R. Pederson, D. J. Singh, C. Fiolhais, *Phys. Rev. B* **1992**, *46*, 6671.

[S19] N. Zhang, A. Jalil, D. Wu, S. Chen, Y. Liu, C. Gao, W. Ye, Z. Qi, H. Ju, C. Wang, X. Wu, L. Song, J. Zhu, Y. Xiong, *J. Am. Chem. Soc*. **2018**, *140*, 9434.

[S20] C. Xie, X. Hu, Z. Guan, X. Li, F. Zhao, Y. Song, Y. Li, X. Li, N. Wang, C. Huang,

Angew. Chem. Int. Ed. **2020**, *59*, 1.

[S21] N. Wang, R. Zhou, H. Li, Z. Zheng, W. Song, T. Xin, M. Hu, J. Liu, *ACS Energy Lett*. **2021**, *6*, 1141.

[S22] W. Sun, C. Zhou, Y. Fan, Y. He, H. Zhang, Z. Quan, H. Kong, F. Fu, J. Qin, Y. Shen, H, Chen, *Angew. Chem. Int. Ed.* **2023**, *62*, e202300158.

[S23] H. Peng, S. Huang, V. Montes-García, D. Pakulski, H. Guo, F. Richard, X. Zhuang, P. Samorì, A. Ciesielski. *Angew. Chem. Int. Ed.* **2023**, *62*, e202216136.

[S24] Y. Lu, X. Hou, L. Miao, L. Li, R. Shi, L. Liu, J. Chen, *Angew. Chem. Int. Ed.* **2019**, *58*, 7020.

[S25] Z. Song, L. Miao, Y. Lv, L. Gan, M. Liu, *Angew. Chem. Int. Ed.* **2023**, *62*, e202309446.

[S26] Q. Sun, T. Sun, J. Du, K. Li, H. Xie, G. Huang, X. Zhang, *Adv. Mater.* **2023**, *35*, 202301088.

[S27] Z. Song, L. Miao, H. Duan, Y. Lv, L. Gan, M. Liu, *Angew. Chem. Int. Ed.* **2024**, *63*, e202401049.

[S28] Z. Song, L. Miao, L. Ruhlmann, Y. Lv, L. Li, L. Gan, M. Liu, *Angew. Chem. Int. Ed.* **2023**, *62*, e202219136.

[S29] N. Patil, C. Cruz, D. Ciurduc, A. Mavrandonakis, J. Palma, R. Marcilla, *Adv. Energy Mater.* **2021**, *11*, 2100939.

[S30] D. Du, J. Zhou, Z. Yin, G. Feng, W. Ji, H. Huang, S. Pang, *Adv. Energy Mater.* **2024**, *14*, 2400580.

[S31] L. Xie, K. Xu, W. Sun, Y. Fan, J. Zhang, Y. Zhang, H. Zhang, J. Chen, Y. Shen, F. Fu, H. Kong, G. Wu, J. Wu, L. Chen, H. Chen, *Angew. Chem. Int. Ed.* **2023**, *62*, e202300372.

[S32] C. Zhang, W. Ma, C. Han, L.-W. Luo, A. Daniyar, S. Xiang, X. Wu, X. Ji, J.-X. Jiang, *Energy Environ. Sci.* **2021**, *14*, 462.

[S33] T. Sun, W. Zhang, Z. Zha, M. Cheng, D. Li, Z. Tao, *Energy Storage Mater.* **2023**, *59*, 102778.

[S34] S. Li, J. Shang, M. Li, M. Xu, F. Zeng, H. Yin, Y. Tang, C. Han, H. Cheng, *Adv. Mater.* **2022**, *34*, 2207115.

[S35] Z. Song, L. Miao, H. Duan, L. Ruhlmann, Y. Lv, D. Zhu, L. Li, L. Gan, M. Liu, *Angew.*

Chem. Int. Ed. **2022**, *61*, e202208821.

[S36] Y. Wang, C. Wang, Z. Ni, Y. Gu, B. Wang, Z. Guo, Z. Wang, D. Bin, J. Ma, Y. Wang, *Adv. Mater.* **2020**, *32*, 2000338.

[S37] M. Tang, Q. Zhu, P. Hu, L. Jiang, R. Liu, J. Wang, L. Cheng, X. Zhang, W. Chen, H. Wang, *Adv. Funct. Mater.* **2021**, *31*, 2102011.

[S38] F. Ye, Q. Liu, H. Dong, K. Guan, Z. Chen, N. Ju, L. Hu, *Angew. Chem. Int. Ed.* **2022**, *61*, e202214244.

[S39] L. Lin, Z. Xue, T. Qiu, J. Zhu, G. Zhang, H. Zhan, K. Wang, X. Sun, *Energy Environ. Sci.* **2024**, *17*, 6499.

[S40] Y. Lin, H. Cui, C. Liu, R. Li, S. Wang, G. Qu, Z. Wei, Y. Yang, Y. Wang, Z. Tang, H. Li, H. Zhang, C. Zhi, H. Lv, *Angew. Chem. Int. Ed.* **2023**, *62*, e202218745.

[S41] Z. Song, Q. Huang, Y. Lv, L. Gan, M. Liu, *Angew. Chem. Int. Ed.* **2025**, *64*, e202418237.

[S42] W. Wang, V. S. Kale, Z. Cao, Y. Lei, S. Kandambeth, G. Zou, Y. Zhu, E. Abouhamad, O. Shekhah, L. Cavallo, M. Eddaoudi, H. N. Alshareef, *Adv. Mater.* **2021**, *33*, 2103617.

[S43] Z. Tie, Y. Zhang, J. Zhu, S. Bi, Z. Niu, *J. Am. Chem. Soc.* **2022**, *144*, 10301−10308.

[S44] Y. Chen, J. Li, Q. Zhu, K. Fan, Y. Cao, G. Zhang, C. Zhang, Y. Gao, J. Zou, T. Zhai, C. Wang, *Angew. Chem. Int. Ed.* **2022**, *61*, e202116289.

[S45] W. Li, H. Xu, H. Zhang, F. Wei, L. Huang, S. Ke, J. Fu, C. Jing, J. Cheng, S. Liu, *Nat. Commun.* **2023**, *14*, 5235.

[S46] L. Luo, C. Zhang, W. Ma, C. Han, X. Ai, Y. Chen, Y. Xu, X. Ji, J. Jiang, *Adv. Mater.* **2024**, *36*, 2406106.

[S47] X. Peng, Y. Xie, A. Baktash, J. Tang, T. Lin, X. Huang, Y. Hu, Z. Jia, D. J. Searles, Y. Yamauchi, L. Wang, B. Luo, *Angew. Chem. Int. Ed.* **2022**, *61*, e202203646.

[S48] G. Studer, A. Schmidt, J. Büttner, M. Schmidt, A. Fischer, I. Krossing, B. Esser, *Energy Environ. Sci.* **2023**, *16*, 3760.

[S49] H. Lv, Z. Wei, C. Han, X. Yang, Z. Tang, Y. Zhang, C. Zhi, H. Li, *Nat. Commun.* **2023**, *14*, 3117.

[S50] X. Ren, D. Tao, S. Cui, T. Li, Y. Cao, F. Xu, *Energy Storage Mater.* **2023**, *63*, 102992.

[S51] C. Han, H. Li, Y. Li, J. Zhu, C. Zhi, *Nat. Commun.* **2021**, *12*, 2400.

[S52] F. Qiao, J. Wang, R. Yu, M. Huang, L. Zhang, W. Yang, H. Wang, J. Wu, L. Zhang, Y. Jiang, Q. An, *ACS Nano* **2023**, *17*, 23046.

[S53] C. Wang, R. Li, Y. Zhu, Y. Wang, Y. Lin, L. Zhong, H. Chen, Z. Tang, H. Li, F. Liu, C. Zhi, H. Lv, *Adv. Energy Mater.* **2023**, *13*, 2302495.

[S54] H. Zhang, D. Xu, F. Yang, J. Xie, Q. Liu, D. Liu, M. Zhang, X. Lu, Y. Meng, *Joule* **2023**, *7*, 971.

[S55] Z. Tie, S. Deng, H. Cao, M. Yao, Z. Niu, J. Chen, *Angew. Chem. Int. Ed.* **2021**, *60*, e202115180.

[S56] N. Wang, Z. Guo, Z. Ni, J. Xu, X. Qiu, J. Ma, P. Wei, Y. Wang, *Angew. Chem. Int. Ed.* **2021**, *60*, 20826.

[S57] Z. Chen, H. Su, P. Sun, P. Bai, J. Yang, M. Li, Y. Deng, Y. Liu, Y. Geng, Y. Xu, *Proc. Natl. Acad. Sci. USA.* **2022**, *169*, e2116775119.